# Genome-wide phage susceptibility analysis in *Acinetobacter baumannii* reveals capsule modulation as a central determinant of phage defense

Jinna Bai[a], Nicole Raustad[a], Jason Denoncourt[a], Tim van Opijnen[b], Edward Geisinger[a]#

[a]Department of Biology, Northeastern University, Boston, Massachusetts, USA

[b] Broad Institute of MIT and Harvard, CISID, Cambridge, Massachusetts, USA

#To whom correspondence should be addressed (e.geisinger@northeastern.edu)

12 **Abstract**

13 Phage have gained renewed interest as an adjunctive treatment for life-threatening infections
14 with the drug-resistant nosocomial pathogen *Acinetobacter baumannii*. Our understanding of the
15 mechanisms used by *A. baumannii* to defend against phage remains limited, although this
16 information could lead to improved antimicrobial therapies. To address this problem, we used
17 Tn-seq to identify determinants of phage susceptibility in *A. baumannii* on a genome-wide scale.
18 These studies focused on the lytic phage Loki, which uses unknown mechanisms to target
19 *Acinetobacter*. We identified 41 candidate loci that increase susceptibility to Loki when
20 disrupted, and 10 that decrease susceptibility. Combined with spontaneous resistance mapping,
21 our results support the model that Loki uses the bacterial capsule as an essential receptor, and
22 that modulation of capsule provides *A. baumannii* with key strategies to control vulnerability to
23 phage. The center of this control is transcriptional capsule regulation by the two-component
24 system BfmRS. Mutations hyperactivating BfmRS simultaneously increase capsule levels and
25 Loki infectivity, while the opposite is true with BfmRS-inactivating mutations. We identified
26 novel BfmRS-activating mutations, including knockouts of an RNase T2 homolog (RnaA) and
27 the disulfide isomerase DsbA, that determine the outcome of a phage encounter. We further
28 found that mutation of a glycosyltransferase (Gtr6) known to modify capsule structure and
29 virulence in clinical strains can also confer complete phage resistance. Finally, additional factors
30 including the outer core of lipooligosaccharide act independently of capsule modulation to
31 interfere with Loki infection. This work demonstrates that regulatory and structural modulation
32 of capsule, known to alter *A. baumannii* virulence, is also a major determinant of susceptibility to
33 phage.

**Author Summary**

Antibiotic-resistant infections with *Acinetobacter baumannii* are a major problem in critical care units and have increased in frequency during the COVID-19 pandemic. The virulence of these infections depends on a polysaccharide capsule surrounding the bacterium. Phage, or viruses that kill bacteria, represent a promising alternative therapy against highly antibiotic-resistant *A. baumannii* infections, and *A. baumannii*-specific phage often target the capsule. Here, we use high-throughput genetics to analyze how *A. baumannii* defends against phage and identify ways to potentiate their killing activity. We found that stressing the bacteria in ways that cause augmented production of capsule also causes hyper-susceptibility to phage. By contrast, turning off the stress response, or mutating the capsule structure, causes complete phage resistance. Altering a second surface structure, lipooligosaccharide, also enhances phage attack. Modulating the amounts or makeup of capsular polysaccharide is known to influence virulence in *A. baumannii*. This work thus uncovers a connection between phage pressure and the evolution of virulence in *A. baumannii*, and it identifies new mechanisms by which the pathogen controls its surface that may be leveraged for improving future phage-based antimicrobial therapies.

49 **Introduction**

50 The antibiotic-resistant, Gram-negative pathogen *Acinetobacter baumannii* is notorious
51 for causing recalcitrant diseases in healthcare settings including sepsis and ventilator-associated
52 pneumonia [1, 2]. Rates of *A. baumannii* infections resistant to last-line antibiotic treatments
53 have increased during the COVID-19 pandemic [3, 4], and pan-resistant isolates have emerged
54 [5, 6]. Therapy with lytic phages (viruses that infect and kill bacterial hosts) has gained renewed
55 attention as an additional line of attack against infections with pathogens such as *A. baumannii*
56 that are refractory to standard antibiotic treatments. Phages have the benefit of having high host
57 specificity, allowing selective targeting of pathogens without broad-spectrum damage to the
58 microbiome. Administration of lytic phages specific to *A. baumannii* strains in animal infection
59 models has been efficacious in protecting the model hosts from disease [4, 7-12]. Moreover,
60 recent successes in the clinic have shown the promise of phage therapy as an adjunct to
61 antibiotics for treating severe, progressive MDR *A. baumannii* infections in critically ill patients
62 [13-15]. Phage may also contribute to measures to block transmission of the pathogen in hospital
63 environments [16].

64 Despite these potential clinical applications, a drawback to phage therapy is the inevitable
65 emergence of bacteria resistant to phage attack [17]. In the case of *A. baumannii* phages, this
66 drawback may be mitigated by tradeoffs associated with phage resistance, such as lowered *in*
67 *vivo* fitness/virulence, enhanced collateral antibiotic sensitivity, or both [12, 17-19]. These costs
68 likely emerge due to *A. baumannii* phages exploiting the bacterial capsule as a requisite receptor
69 for initiating infection [20-23].

70 Capsular polysaccharide is one of the most important virulence factors of *A. baumannii*
71 [24-26]. Acapsular escape mutants isolated after phage treatment in animal models show

72 dramatic attenuation similar to that documented for engineered capsule-null strains [12, 17, 18].
73 Although almost all *A. baumannii* patient isolates produce a capsule, the sugar compositions and
74 structures of the capsular polysaccharide have diversified greatly across strains [27, 28]. These
75 differences are in large part based on substitution of multiple genes within the highly variable K
76 locus, which determines subunit sugar synthesis, polymerization, and export of the capsular
77 polysaccharide [29, 30]. In some cases, structural changes can also manifest from variation in a
78 single gene in the K locus [26, 31]. Different capsule structures may influence the interface with
79 the host innate immune system, resulting in differences in how the capsule promotes
80 pathogenicity [26, 32-34]. In addition to structural variation across strains, *A. baumannii* varies
81 the amount of capsule produced through regulatory networks. These capsule control networks
82 include those that sense and respond to antimicrobial stress [35, 36] or that stochastically switch
83 bacteria between two distinct phenotypic states [37-39], and each may contribute to how bacteria
84 adjust to changing host or environmental conditions. The degree to which modulation of capsule
85 levels affects susceptibility to phage attack is not known. Similarly, whether low-cost mutations
86 modifying (rather than eliminating) capsule can provide avenues to phage resistance is also
87 unclear. More broadly, functional characterization of *A. baumannii* determinants that facilitate or
88 impede phage infection is largely lacking. Knowledge of these features could lead to strategies
89 for improving the efficacy of anti-*A. baumannii* phage therapy and could enhance our
90 understanding of the physiology and resilience of the organism.
91 Here, we use a functional genomic approach to investigate determinants of *A. baumannii*-
92 phage interactions. We use Loki (vB_AbaS_Loki), a lytic phage of the *Siphoviridae* family
93 initially isolated from activated sewage sludge that targets *A. baumannii* by unknown
94 mechanisms [40]. These studies allowed us to identify the Loki host receptor, the K3/K22

95 capsule, and to reveal the key function of capsule modulation in determining the outcome of
96 phage interactions. This work has implications for phage therapy against *A. baumannii* and for
97 understanding the interplay between phage pressure and development of virulence in the
98 pathogen.
99

100 **Results**

101 **High-throughput identification of phage susceptibility determinants in *A. baumannii*.**

102 Loki infects *A. baumannii* reference strain ATCC 17978 [40], forming small, turbid
103 plaques on solid medium and resulting in partial growth inhibition in liquid culture when using
104 an initial multiplicity of infection (MOI) of 1 or 10 (Fig 1A). We took advantage of these
105 features to investigate the genetic determinants of phage susceptibility in the host bacterium by
106 Tn-seq, using the strategies we have established for identifying determinants of susceptibility to
107 antibiotics [41, 42]. Ten independent *Mariner* insertion pools each having about 20,000
108 individual insertions [43] (~100,000 separate insertion sites in total) were grown for ~8
109 doublings in parallel in broth containing Loki at different MOIs (1 to 1.5, or 10 to 15), or no
110 phage (uninfected control). DNA was extracted from samples before ($t_1$) and after ($t_2$) the
111 outgrowth of each pool. The frequency of every transposon mutant in the population at each time
112 point was then determined by massively parallel sequencing, followed by calculation of each
113 mutant's relative fitness [41, 42] (see Materials and Methods). We then aggregated all the mutant
114 fitness values associated with each gene across all pools to determine an average, gene-level
115 fitness score for a given condition (S1 Dataset). Genes were identified that had decreased or
116 increased Tn-seq fitness during phage challenge, based on established criteria [fitness value
117 derived from n ≥ 3 independent insertion mutants, fitness difference ≥ 10%, and false-discovery

118 rate (FDR) ≤ 0.05 [41, 42]] (see Materials and Methods). These genes and their products are
119 defined operationally as candidate phage susceptibility determinants, and those associated with
120 decreased fitness upon phage challenge when mutated are referred to as candidate phage
121 hypersusceptibility determinants.

122 Challenge with Loki at the lower MOI (1 to 1.5) resulted in 14 candidate phage
123 hypersusceptibility determinants (Fig 1B and S1 Dataset). The hits comprised numerous proteins
124 involved in biosynthesis and control of the bacterial cell envelope. These included *bfmS*, the
125 receptor of the virulence/resistance regulatory BfmRS two-component system (TCS), which
126 regulates capsule production [35, 36, 44]; lipooligosaccharide (LOS) core oligosaccharide
127 biosynthesis genes (*gtrOC2*, *gtrOC3*, *pda1*, *gtrOC4*, and *lpsB*) [29, 41]; and the *dsbA* dithiol
128 oxidase [45] critical for forming protein disulfide bonds in the Gram-negative periplasm [46] (S1
129 Data Set). Additional hits were ACX60_RS02390 (referred to hereafter as *rnaA*), encoding a
130 predicted periplasmic RNase T2 homolog; the *lon* protease; and the *dksA* transcription factor
131 known to affect lytic phage infection in *E. coli* [47, 48].

132 Challenge with Loki at higher MOI (10 to 15) expanded the number of
133 hypersusceptibility determinants to 39, and also resulted in hits that had increased fitness (i.e.,
134 decreased susceptibility) in the face of Loki challenge (Fig 1B and S1 Dataset). The expanded set
135 of hypersusceptibility hits included additional enzymes belonging to the functional categories
136 above (e.g., disulfide bond formation, *dsbC*, *dsbD*; LOS synthesis, *gtrOC8*; and the protease
137 *clpA*), as well as additional functional categories associated specifically with the higher MOI
138 (e.g., the DNA adenine methyltransferase, *aamA* [49]). Regarding the hits having increased
139 fitness during Loki challenge, the strongest of these was *gne1*, which is part of the K locus and
140 encodes an epimerase generating UDP-linked sugar precursors for capsule biosynthesis [29].

141 Loss of Gne1 completely prevents capsule production [50]. An additional K locus gene, *gtr9*,
142 mutation of which is also linked to capsule loss [19], also caused increased fitness during Loki
143 challenge when mutated (S1 Dataset). The other hits were extrinsic to the K locus, but several
144 had annotations related to polysaccharide production. The Tn-seq screen thus reveals a variety of
145 candidate factors that increase or decrease *A. baumannii* vulnerability to phage attack.
146

147 **Targeted deletion and complementation analyses validate the phage hypersusceptibility**
148 **phenotypes predicted by Tn-seq.**

149 We confirmed the Tn-seq results using individual mutant strains, focusing first on
150 candidate phage susceptibility determinants from different functional categories showing lower
151 Tn-seq fitness with Loki challenge (Fig 2A). Strains carrying in-frame deletions of *rnaA*, *dsbA*,
152 *gtrOC3*/*4*, and *lon* were constructed (Materials and Methods). To enable *trans* complementation
153 analysis, plasmids harboring an IPTG-inducible WT allele of each gene, or a control plasmid
154 lacking the gene, were introduced into the respective mutant strains (S1 Table). In the case of
155 *bfmS*, in lieu of complementation analysis we used two different mutants isolated previously—a
156 deletion with *aacC1* replacement (referred to as Δ*bfmS*), and the spontaneous frame-shift mutant
157 G467Dfs*19 [35] (referred to as *bfmS**)—as well as additional mutants within the *bfmRS* locus
158 as will be explained in a subsequent section. Susceptibility to Loki was assessed by liquid
159 infection and plaque formation assays (Materials and Methods). With liquid phage challenge, the
160 *rnaA*, *dsbA*, and *bfmS* mutants all showed complete block of growth immediately after exposure
161 to Loki, unlike the WT, which showed partial growth inhibition manifesting mostly after about
162 5h (Fig 2B and C). Different kinetics were seen with Loki challenge of the other mutants. With
163 the Δ*gtrOC3* and Δ*gtrOC4* mutants exposed to phage, the population grew for an initial ~2.5 h

164 before collapse of bacterial density (Fig 2B). With Δ*lon*, by contrast, little growth occurred in the
165 presence of Loki until ~4h, at which point rapid bacterial growth resumed (Fig 2B).
166 Reintroduction of the respective WT genes reversed the Loki hypersusceptibility phenotypes of
167 *rnaA, dsbA*, *gtrOC3*, *gtrOC4*, and *lon* mutants. In some cases, leaky expression without IPTG
168 was sufficient for partial (*dsbA*, *gtrOC4*) or full (*gtrOC3, lon*) complementation (Fig 2B).
169 Addition of IPTG at 0.1 mM allowed reversal of the Loki hypersusceptibility phenotype with all
170 strains, although a partial growth delay defect remained with the *rnaA* reintroduction strain
171 exposed to phage (Fig 2B). Raising the level of *rnaA* induction by using 1 mM IPTG completely
172 eliminated this defect, and had the added effect of making the *rnaA* reintroduction strain even
173 less susceptible to Loki than the WT control (Fig 2D).
174 Results from plaque formation assays mirrored the findings from the liquid challenge
175 experiments. While Loki interaction with the WT control resulted in small, turbid plaques, each
176 candidate hypersusceptibility mutant permitted large, clear plaques and zones of complete lysis
177 at areas of high phage concentration (Fig 2E and F). Plaques appeared to be larger with *rnaA,*
178 *dsbA*, and *bfmS* mutants compared to *gtrOC3* and *gtrOC4*, echoing the susceptibility differences
179 of the same strains during Loki challenge in broth (Fig 2, compare E, F to B, C.). Expressing the
180 respective genes *in trans* with 1 mM IPTG reversed the enhanced plaque formation phenotypes
181 in all cases (Fig 2E), with cloned *rnaA* greatly lowering the plaque formation efficiency of
182 Δ*rnaA* beyond the level of the WT control, agreeing with the findings with liquid infection (Figs.
183 2D and 2E, compare Δ*rnaA*/*rnaA* to the WT control).
184 We note that the gene directly upstream of *rnaA*, ACX60_RS02385 (*slt* [36]), was also
185 identified as a candidate susceptibility determinant associated with modestly decreased fitness
186 during Loki challenge (S1 Dataset). Exposure of an in-frame Δ*slt* mutant to Loki recapitulated

187 the modest hypersusceptibility defect (S1A, B Fig). Analysis of the Tn-seq mutant fitness
188 profiles within *slt* revealed a potentially biased distribution, with insertions causing major Loki
189 hypersusceptibility defects having an apparent bias toward the 3' end of the locus that is
190 proximal to *rnaA* (Fig 2A). The Δ*slt* mutant also showed slightly reduced levels of *rnaA*
191 expression (S1C Fig). Since phage susceptibility appears sensitive to *rnaA* expression level (Fig
192 2B, D, E), we cannot rule out a polar effect on *rnaA* in the altered phage susceptibility of the *slt*
193 mutant, and this mutant was not pursued further. These results underscore that candidate Loki
194 hypersusceptibility loci identified through Tn-seq show the predicted susceptibility phenotypes
195 when analyzed independently using engineered mutant strains.
196
197 **Analysis of Loki resistance mutations reveals capsular polysaccharide as phage receptor.**
198 Given the identification of capsule production genes as sites of mutations that increase fitness in
199 the presence of phage challenge (S1 Dataset), we tested the hypothesis that the capsule is
200 essential to the infective cycle of Loki by serving as a host receptor. To this end, we examined
201 the Tn-seq data associated with the entire K locus of ATCC 17978 (KL3) and additional genes
202 involved in capsule production. Gene-level Tn-seq fitness scores were available for 9 out of 20
203 KL3 genes, with the others being represented by too few transposon mutants due to their
204 essential involvement in late steps of capsule biosynthesis [43]. Transposon disruption of most of
205 the 9 permissive KL3 genes led to higher fitness (*W*) during Loki exposure relative to untreated
206 control (with 5 having non-FDR $P < 0.05$; Fig 3A). Disruption of *wzi*, an additional permissive
207 gene outside the K locus that encodes the lectin required for efficient surface binding of exported
208 capsular polysaccharide [51], also increased Tn-seq fitness during Loki challenge compared to
209 control, albeit without passing statistical cut-offs ($P = 0.15$). Since a subset of the glycan

210 building blocks encoded by the K locus are used for protein glycosylation by PglL [52], we also
211 examined the *pglL* Tn-seq phenotypes. In contrast to the capsule synthesis genes, transposon
212 insertions in *pglL* showed slightly decreased fitness during Loki challenge (Fig 1A). These
213 findings indicate that lesions leading to capsule deficiency are associated with enhanced fitness
214 in the face of Loki challenge, while the opposite is true for *pglL* mutations, which are known to
215 eliminate protein O-glycans but preserve capsule [52].

216 Building on these observations, we examined the requirement of capsule for Loki
217 infection by using (1) gene deletions, (2) additional clinical isolates of known capsule types, and
218 (3) spontaneous phage-resistant mutants. First, we analyzed deletions in ATCC 17978 of two
219 critical capsule synthesis genes: *itrA*, the initiating transferase required for use of phosphosugars
220 in both capsule synthesis and protein O-glycosylation and *wzc*, essential to assembly and export
221 of high-molecular weight capsular polysaccharide[29, 35, 52]. The effects of Δ*itrA* reflect loss of
222 both capsule and protein O-glycans, while Δ*wzc* reflects loss of capsule specifically. We note
223 that unlike *itrA*, *wzc* is essential in ATCC 17978 [35, 43]. Δ*wzc* could be analyzed, however, by
224 the parallel use of EGA106-27, which is a viable Δ*wzc* isolate harboring extragenic
225 compensatory mutations, and EGA260, its isogenic *wzc*-repaired derivative obtained by marker
226 rescue [35]. As predicted by Tn-seq, deletion of *itrA* led to increased growth during Loki
227 challenge in liquid (S2 Fig) and solid medium (Fig 3B), with plaque formation completely
228 blocked in the latter. Reintroduction of *itrA* reversed this defect, with the resulting susceptibility
229 to Loki dependent on the level of *itrA* induction (Fig 3B; S2 Fig). Loki was also completely
230 unable to form plaques on EGA106-27 ($Wzc^-$), but formed plaques readily on EGA260 ($Wzc^+$).
231 These plaques were larger and clearer than with the WT host, presumably a consequence of the
232 compensatory mutations rendering EGA260 hypersensitive to phage. The Loki non-susceptibility

233 of ItrA-deficient (capsule$^-$/protein O-glycan$^-$) and Wzc-deficient (capsule$^-$/protein O-glycan$^+$)
234 strains, and the hypersusceptibility detected with *pglL* transposon mutants (capsule$^+$/protein O-
235 glycan$^-$), emphasizes the importance of the polysaccharide capsule for phage infection.
236 Second, we found that Loki infects unrelated clinical isolates bearing the same capsule
237 type as ATCC 17978, but not isolates of a structurally distant type, consistent with capsule
238 providing a specific host receptor. ATCC 17961 and ATCC 19606, which both belong to the
239 same KL3 capsule type as ATCC 17978 [27, 53], supported Loki infection (Fig 3C). ATCC
240 19606 infection resulted in turbid lysis in areas where Loki was spotted at low dilutions without
241 detectable plaques at high dilutions (Fig 3C). A Δ*bfmS* mutant of ATCC 19606, however,
242 permitted high efficiency plaque formation by Loki (Fig 3C). By contrast, Loki was unable to
243 form plaques on strain AB5075, which produces a KL25-type capsule [54], regardless of
244 presence of a *bfmS* mutation (Fig 3C). These results highlight the importance of capsule type in
245 permitting Loki infection, and support a potential interaction between *bfmS* and capsule in
246 promoting phage hypersusceptibility.
247 As a third test of the model that capsule provides an essential receptor for Loki, we
248 isolated spontaneous Loki-resistant mutants. Three independent mutant ATCC 17978 colonies
249 forming within zones of confluent lysis were purified and analyzed by whole-genome
250 sequencing (Materials and Methods). Each strain had a single, slipped-strand mispairing
251 mutation within homopolymeric sites in the K locus (Fig 3D). Two had identical mutations in
252 *gtr6* (440$A_{9\rightarrow 8}$), encoding a glycosyltransferase that adds a single sugar side-chain to the capsule
253 repeat unit [26] (S2 Table), and the third had a mutation in the *wzx* polysaccharide flippase
254 (377$T_{9\rightarrow 10}$) [29]. Each mutation caused a frameshift resulting in premature translation
255 termination. While deficiency of Wzx is expected to result in complete capsule loss, Gtr6

256 deficiency is known to preserve capsule but cause an altered structure lacking the side chain
257 sugar [26]. Intriguingly, *gtr6* deletion was recently shown to amplify virulence in ATCC 17978
258 in a bacteremic disease model, and a naturally occurring *gtr6* mutation (1008::IS*Aba13*) was
259 found to drive hypervirulence in a highly pathogenic clinical isolate (HUMC1) with a related K
260 locus (KL22) [26]. We confirmed that the ATCC 17978 *gtr6*440A$_{9\rightarrow 8}$ mutant resists Loki plaque
261 formation, a phenotype reversed by expression of the WT allele in trans (Fig 3E) and
262 recapitulated by an in-frame *gtr6* deletion (Fig 3F). Consistent with previous findings that loss of
263 Gtr6 alters capsule structure but not amount [26], *gtr6*440A$_{9\rightarrow 8}$ and Δ*gtr6* caused no change to
264 overall capsule levels (S3 Fig). Search of public databases revealed that the 440A$_{9\rightarrow 8}$ allele is
265 present in a variety of *A. baumannii* clinical isolates bearing KL3 or 22 (S2 Table), consistent
266 with this site as a mutational hotspot in *gtr6*. We also examined the *gtr6* locus from the genomes
267 of two KL22 strains within our *A. baumannii* clinical isolate collection, EGA10 and EGA65.
268 While the 440A$_{9\rightarrow 8}$ allele was not present, we found a novel IS*Aba13* insertion near this site
269 (*gtr6*425::IS*Aba*13) in both strains, resembling the situation with HUMC1 [26]. EGA10 and
270 EGA65 were both resistant to Loki, but introducing *gtr6* (WT) from ATCC 17978 via plasmid
271 had the dramatic effect of engendering Loki susceptibility with efficient plaque formation (Fig
272 3E). These results suggest that *gtr6* is a hub for phage-evasion mutations, and point to a potential
273 relationship between phage evasion and the collateral evolution of increased virulence in *A.*
274 *baumannii* clinical strains.

275 To solidify the capsule receptor model, we examined the effect of *itrA*, *gtr6*, and *wzc*
276 mutations on phage adsorption (Materials and Methods). Each mutation resulted in loss of Loki
277 attachment, as indicated by high fractions of phage remaining in suspension after mixture with

278 bacteria (Fig 3G). Together these results support the conclusion that Loki uses the K3/K22
279 capsule as an essential receptor.
280
281 **BfmRS activity controls Loki susceptibility.**
282 Loki-hypersensitizing *bfmS* mutations are known to lead to capsule hyperproduction via
283 enhanced transcription of K locus genes [35], and could thereby also control susceptibility to
284 phage. We tested this model by analyzing mutations in *bfmR*, which are known to cause
285 decreased capsule production [35]. BfmR$^-$ strains are thus predicted to show decreased
286 susceptibility to capsule-targeting phage. In the Tn-seq screen, *bfmR* transposon mutants indeed
287 had increased fitness during Loki challenge relative to controls, particularly at the higher MOIs,
288 in stark contrast to the dramatic hypersusceptibility of *bfmS* mutants (Fig 4A). To confirm the
289 altered phage susceptibility phenotype associated with *bfmR*, we used a knockout of the entire
290 TCS (Δ*bfmRS*), which phenocopies a single *bfmR* deletion [35, 36, 44] and shows reduced
291 capsule levels compared to WT and the hyper-encapsulated *bfmS** mutant (Fig 4B). As predicted
292 by Tn-seq, Δ*bfmRS* is impervious to Loki in both liquid infection and plaque formation assays
293 (Fig 4C, D). Given this non-susceptibility and the epistatic relationship of BfmR to BfmS, we
294 predicted that spontaneous phage-resistance mutants of hypersusceptible BfmS$^-$ strains would
295 map to *bfmR*. To this end, mutant colonies derived from *bfmS** that formed within zones of lysis
296 by Loki were purified and analyzed by whole-genome sequencing. In two independent mutants,
297 the resistance mutations were indeed in *bfmR*, causing amino acid substitutions G100D and T85I.
298 Each of these mutations completely prevented Loki infection in either liquid (Fig 4C) or plaque
299 (Fig 4E) assays, despite the hypersusceptibility of the parent strain. G100 and T85 are highly
300 conserved and are near the BfmR dimerization interface and the predicted site of

301 phosphorylation, respectively, based on the published crystal structure [55, 56]. The mutations
302 are thus predicted to inactivate BfmR, with T85I, in particular, corresponding exactly to a
303 described mutation in the "switch" residue of *E. coli* CheY (T87I) that blocks its
304 phosphorylation-induced conformational changes and activation [57]. Consistent with loss of
305 function, both BfmR substitutions greatly reduced the phosphorylated (predicted active [44])
306 fraction of the protein (BfmR~P, Fig 4F) (Materials and Methods), and lowered capsule
307 production to levels equivalent to that seen with Δ*bfmRS* (Fig 4B). We note that in addition to
308 *bfmR*, other sequenced BfmS$^-$ Loki-escape mutations again mapped to *gtr6*, including two
309 independent *gtr6*440A$_{9\rightarrow 8}$ mutations and another, novel slipped-strand mispairing mutation
310 within a different, nearby poly-A tract (*gtr6*384A$_{8\rightarrow 7}$) (Fig 3D, S2 Table).
311 The opposing effects on capsule levels and Loki susceptibility in BfmR$^-$ (low capsule,
312 low infectivity) and BfmS$^-$ (high capsule, high infectivity) mutants suggests that regulation of the
313 capsule receptor determines the differential sensitivity to Loki in each strain. In agreement with
314 this model, compared to WT, Loki showed reduced adsorption to Δ*bfmRS* and dramatically
315 increased adsorption to *bfmS** (slow vs rapid decline in the fraction of free phage, respectively,
316 Fig 4G). The increased adsorption and infectivity of Loki with BfmS$^-$ bacteria still relied on an
317 intact K3 capsule, as deleting *itrA* or *gtr6* in a BfmS$^-$ background led to dramatic loss of Loki
318 adsorption (S4A Fig) and killing (S4B Fig). These data thereby further support the notion that
319 the BfmRS-dependent boost in Loki susceptibility depends on capsule.
320
321 **Defects in RnaA and DsbA control Loki susceptibility through BfmRS-mediated capsule**
322 **regulation**

323 We reasoned that additional lesions uncovered in our genome-wide screen may owe their
324 altered Loki susceptibility phenotypes to modulation of the capsule receptor. We found that
325 knockouts of *rnaA* and *dsbA*, which lead to hypersusceptibility phenotypes, also each showed
326 increased capsule production (by ~50%, Fig 5A) and Loki surface adsorption (Fig 5B), similar to
327 the enhancements caused by the Loki-hypersensitizing *bfmS* mutation (Fig 4B, G). As expected,
328 augmented capsule production was reversed by expressing each WT allele in trans (S5A Fig).
329 Consistent with the capsule increase occurring as a result of a regulatory response, the Δ*rnaA* and
330 Δ*dsbA* mutants each showed increased transcription of capsule biosynthesis genes (*wza* and
331 *gnaA*, Fig 5C). Given the importance of the BfmRS capsule regulator in determining the
332 outcome of the Loki-*A. baumannii* interaction, and the identical capsule and phage susceptibility
333 phenotypes shared by *rnaA*, *dsbA*, and *bfmS* mutants, a prime candidate for mediating this
334 response is BfmRS. We thus defined the epistatic relationship of *bfmRS* with *rnaA* and *dsbA* in
335 determining Loki susceptibility. We found that combining Δ*rnaA* or Δ*dsbA* with Δ*bfmRS* led to
336 low capsule levels (at or below the level seen with Δ*bfmRS*, Fig 5A) and complete resistance to
337 phage attack in both liquid challenge and plaque formation assays (Fig 5D, E), mirroring the
338 Δ*bfmRS* single mutant phenotypes (Fig 4). The results are consistent with the *rnaA* and *dsbA*
339 mutations acting through BfmRS to cause enhancements to capsule and phage susceptibility.
340 We observed in previous complementation experiments that in-trans overexpression of
341 *rnaA* in a Δ*rnaA* strain led not only to a reversal of the mutant's hypersusceptibility and capsule
342 defects, but also to further decreases in susceptibility and capsule levels compared to the WT
343 control, effects not seen with the analogous *dsbA* reintroduction (Fig 2E; S5A, B Fig). We took
344 advantage of these effects to further probe the linkage between RnaA modulation of phage
345 susceptibility and BfmRS-mediated regulation of capsule. We predicted that the lowered Loki

346 susceptibility caused by high RnaA levels would be mediated through capsule down-regulation
347 by BfmRS. Indeed, we found that overexpressing *rnaA* in trans via 1mM IPTG in a WT strain
348 led to lower levels of capsule compared to the uninduced control (Fig 5F), and completely
349 prevented Loki plaque formation (Fig 5G). Both of these effects were blocked when *rnaA*
350 induction occurred in a *bfmS** strain harboring the inactive version of the BfmS TCS receptor
351 (Fig 5F, G). In contrast to the results with *rnaA* and as predicted from Fig 2E, overexpressing
352 *dsbA* in a WT strain did not inhibit plaque formation (S5C Fig). These results are consistent with
353 the model that RnaA levels are sensed by BfmRS, leading to up-regulation (low RnaA) or down-
354 regulation (high RnaA) of capsule, the Loki receptor. Presence vs absence of DsbA function, but
355 not its relative levels, is likely similarly sensed.

356 Several additional lines of evidence support the model that defects associated with RnaA
357 and DsbA are sensed by BfmRS. First, we found that Δ*rnaA* and Δ*dsbA* both activate a BfmRS-
358 dependent transcriptional green fluorescent protein (GFP) reporter (18040p-GFP [36]), resulting
359 in ~6-fold increase in reporter levels (Fig 6A, left). Similar increases were not seen with a
360 different reporter, *adc*p-GFP, whose activity is BfmRS-independent [36] (Fig 6A, right), or with
361 18040p-GFP when Δ*rnaA* or Δ*dsbA* were combined with Δ*bfmRS* (Fig 6B). These results
362 indicate that reporter enhancement by RnaA and DsbA deficiency is specific and dependent on
363 BfmRS. Second, Δ*rnaA* and Δ*dsbA* each increased the fraction of BfmR~P by approximately 3-
364 fold, similar to the effect of *bfmS* deletion (Fig 6C). Third, analysis of previous genome-wide
365 fitness datasets [41] revealed that *rnaA*, *dsbA,* and *bfmS* mutants have highly correlated antibiotic
366 susceptibility profiles (phenotypic signatures), which are likely to reflect functional connectivity
367 between the genes (Fig 6D and S5D Fig, $r = 0.58\text{-}0.67$, $p < 0.0005$). The *bfmS*, *rnaA*, and *dsbA*
368 signatures were also positively correlated with those of other Dsb system homologs in *A.*

369 *baumannii* (DsbB, DsbD, and at least one of 3 DsbC paralogs, ACX60_RS16880), suggesting
370 that disulfide bond formation in general is linked to the functions of BfmS and RnaA. Mutations
371 in *dsbB*, *dsbD* and the same *dsbC* paralog (RS16880) also showed decreased Tn-seq fitness
372 during Loki challenge, albeit not to the degree seen with *dsbA* (Fig 6E). Fourth, our previous
373 RNA-seq data [36] showed that expression of several *dsb* genes as well as *rnaA* is under the
374 control of BfmRS, with BfmR$^-$ and BfmS$^-$ mutants having differential effects on their
375 transcription (S5E Fig). Finally, while the Δ*rnaA*, Δ*dsbA*, and Δ*bfmRS* individual mutants and
376 the Δ*rnaA* Δ*bfmRS* combined mutant do not show substantially impaired growth at 37°C, we
377 found that combining Δ*dsbA* and Δ*bfmRS* results in a synthetic growth defect (Fig 6F). This
378 result implies that BfmRS protects *A. baumannii* from DsbA deficiency and the consequent
379 defects in periplasmic protein disulfide bonds, consistent with a toxicity-stress response
380 relationship.

381 Like the disulfide bond formation enzymes, the relationship between RnaA, an RNase-
382 domain protein, and BfmRS activation was previously unknown. The ortholog of *A. baumannii*
383 RnaA in *E. coli* is RNase I, a periplasmic enzyme. RnaA also contains a signal peptide (Fig 7A),
384 and a fusion to a monomeric superfolder GFP (msGFP2) localized to discrete foci at the cell
385 periphery (Fig 7B,C), consistent with placement in the periplasm. *rnaA-msGFP2* reversed Δ*rnaA*
386 hypersusceptibility to Loki, mimicking the effect of the WT allele and indicating that the fusion
387 protein is functional (S5F Fig). RnaA is also similar to RNase I in its possession of eight cysteine
388 residues (Fig 7A) potentially facilitating internal disulfide bonds [58]. Unlike RNase I, however,
389 RnaA and its close orthologs within *Acinetobacter* and *Psychrobacter* completely lack the
390 catalytic histidines and other key residues in its two conserved active sites (CAS) (Fig 7A) [59],
391 as previously noted with the *A. baumannii* RnaA sequence [60]. These findings suggest that

392 RnaA may be a pseudoenzyme, whose levels and/or folding in the periplasm may influence
393 BfmS signaling and phage susceptibility.
394
395 **Factors influencing phage infection independent of capsule modulation**
396 While modulation of capsule is a major feature controlling Loki susceptibility, we found
397 that other hypersusceptibility determinants—including *gtrOC3*, *gtrOC4*, and *lon*—affect
398 vulnerability to Loki independently of regulating the capsule receptor. Deletions of these genes
399 resulted in growth defects during phage challenge in liquid medium that were characterized by
400 different kinetics compared to those of the hypo-encapsulated *rnaA*, *dsbA*, and *bfmS* mutants (Fig
401 2B, C), consistent with an alternate mechanism underlying their susceptibility defects.
402 Deletions of *gtrOC3* and *gtrOC4*, which encode predicted LOS outer core
403 glycosyltransferases [29], resulted in the expected enrichment of truncated forms of LOS (Fig
404 8A), without lowering the overall amount of LOS produced (Fig 8B). The deletions also showed
405 no change to the levels or size distribution of capsular polysaccharide compared to the WT
406 control (Fig 8C, D). Despite having WT levels of the capsule receptor, the Δ*gtrOC3* and
407 Δ*gtrOC4* mutants both showed similar enhancements to Loki adsorption, particularly at the later
408 10 and 20 minute time points (Fig 8F). As noted previously, additional LOS outer core synthesis
409 genes showed decreased fitness during Loki challenge compared to controls (Fig 8E, S1
410 Dataset). This suggests that a range of lesions affecting the LOS outer core can affect Loki
411 susceptibility, with *gtrOC3* and *gtrOC4* mutants likely leading to the most pronounced defects.
412 By combining Δ*gtrOC3* with additional mutations, we found that the enhanced Loki attachment
413 and susceptibility of the LOS outer core mutant still depended on initial binding to capsule. A
414 Δ*gtrOC3* Δ*itrA* double mutant showed complete lack of Loki adsorption (Fig 8G), and Δ*gtrOC3*

415 Δ*itrA* and Δ*gtrOC3* Δ*gtr6* double mutants showed full phage resistance in plaque formation and
416 liquid infection assays (Fig 8H, I). The full-length LOS outer core thus functions to inhibit the
417 ability of Loki to efficiently adhere to and infect *A. baumannii*, likely after the initial requisite
418 interaction with capsule.

419 Deleting *lon* caused no significant change to capsular polysaccharide levels (S6A Fig),
420 consistent with previous observations [61], and had no effect on LOS quantity or banding pattern
421 (S7E, F Fig). As predicted from the lack of major changes to the key surface components, Loki
422 adsorption was not significantly enhanced with the Δ*lon* mutant vs WT; rather, adsorption
423 appeared lowered at the early 5-min time point compared to WT (S6B Fig). Lon protease may
424 thus be affecting susceptibility to Loki by influencing a lytic cycle step occurring after surface
425 interactions.

426 We considered the possibility that the altered Loki susceptibility of mutants showing
427 altered capsule production could also involve alterations to LOS. We therefore examined LOS
428 from the *bfmRS*, *bfmS*, *rnaA* and *dsbA* deletion mutants. LOS from Δ*bfmRS*, Δ*rnaA* and Δ*dsbA*
429 showed no differences in banding pattern or total levels compared to LOS from WT (S7A-D
430 Fig). With Δ*bfmS*, while overall LOS amounts were not significantly altered, we observed the
431 appearance of a single, novel band migrating slightly faster than the full-length LOS (S7A Fig,
432 arrowhead). This band may represent an LOS intermediate, although it is slower migrating and
433 much less abundant than the major intermediate band enriched in Δ*gtrOC3* and Δ*gtrOC4*
434 mutants. Thus, while it is likely that the capsule regulatory mutants owe their altered Loki
435 susceptibility principally to changes in the abundance of capsule, a contribution of altered LOS
436 to the dramatic hypersusceptibility of *bfmS* mutant strains cannot yet be ruled out.
437

438 **Discussion**

439 Bacteriophage show promise as an alternative therapy against *A. baumannii*, but the
440 innate mechanisms controlling vulnerability to phage attack are poorly understood. In this work
441 we have globally analyzed the determinants of defense against an *A. baumannii* phage (Loki)
442 using Tn-seq. This approach led to the identification of capsule as the adsorption receptor and the
443 finding that capsule regulation by BfmRS and novel associated proteins allow control of phage
444 predation. Alteration of capsule structure through naturally occurring glycosyltransferase
445 mutations was also found to provide phage resistance. Many characterized *A. baumannii* phages
446 depend on specific host capsular polysaccharides, and capsule modulation is connected to altered
447 virulence [26, 35-38]. The capsule-linked susceptibility mechanisms may thus have potentially
448 broad relevance for combatting the opportunistic pathogen. Additional determinants of
449 susceptibility both at and downstream of the cell surface were also uncovered, identifying
450 multiple points of vulnerability that may be targeted to potentiate phage attack.

451 That capsule structural modulation mediates phage escape has implications for strategies
452 to control the evolution of phage resistance and virulence. Mutations in *gtr6*, which determines
453 the addition of N-acetyl-β-D-glucosamine branches on the K3/K22 capsule backbone [26], are
454 known to be naturally occurring in clinical isolates and to increase virulence [26]. Our findings
455 thus suggest that phage, in the environment or during therapy, may impose selective pressures
456 that could facilitate the evolution of altered capsules with the undesired collateral effect of
457 increased pathogenicity. Notably, a repeat region within another predicted side-chain
458 glycosyltransferase, *gtr76*, was a site of mutations in phage-resistant K116 *A. baumannii* isolated
459 from a patient receiving phage [23], although effects on capsule structure were not determined.
460 Mutational capsule loss is an additional, well-described phage escape mechanism usually

461 associated with lowered *in vivo* fitness and other trade-offs, making this form of resistance an
462 appealing target of sequential or combination therapies exploiting the trade-offs [18, 62]. Our
463 data, and potentially those of [23], argue that capsule-loss mutations should not be considered a
464 universally predictable path of phage resistance and that capsule-altered mutants with maintained
465 or enhanced virulence should also be considered. This may be especially relevant when targeting
466 particular capsules, such as K3/K22. Phage with broadened specificity for both Gtr6$^{+}$ and Gtr6$^{-}$
467 capsules may allow targeting of K3/K22 *A. baumannii* while blocking the rise of undesired
468 mutants. In sum, these observations support the notion that prior research into resistance
469 mechanisms can enhance the predictability of bacterial evolution during phage exposure and may
470 allow improvements to the therapeutic uses of phage [18, 23, 62].
471 Controlling the abundance of capsule is also tightly connected to modulation of
472 virulence, and we show here that this control has the additional effect of modulating phage
473 susceptibility, with implications for developing phage-drug synergies [62-64] and for
474 understanding variable capsule production in the pathogen. *A. baumannii* regulates capsule
475 production through multiple mechanisms, including the BfmRS stress response and stochastic
476 phenotypic switching systems, and the regulatory states associated with higher capsule
477 production show increased virulence [35-38]. We show that capsule-overproducing mutants
478 hyperactive in BfmRS cause increased adsorption to and killing by capsule-targeting phage.
479 Future work will test the possibility that antimicrobials that increase capsule [35] could
480 potentiate killing by capsule-targeting phages, while the opposite may be seen with antagonists
481 of capsule production. Chemical inhibitors of DsbA function [46, 65], which would amplify
482 capsule through BfmRS signaling while impairing envelope proteins generally, represents an
483 attractive candidate class of small-molecule phage potentiators. Regarding the basis of variable

484 capsule production, our results raise the possibility that environmental phage are among the
485 putative selective pressures that enrich low-capsule (translucent) variants arising from stochastic
486 phenotype switching [37].

487 By examining determinants of Loki susceptibility that modulate capsule through BfmRS,
488 this work provides new leads into the signals detected by the virulence-resistance regulator,
489 which have remained poorly defined. We reveal that changes in DsbA and RnaA generate
490 signals sensed by the TCS, leading to changes in the putative active BfmR~P component and
491 transcriptional control of biosynthesis of capsule, the phage receptor. The finding that lesions
492 affecting periplasmic disulfide bonds generate a stress-response has a parallel in the *E. coli* Cpx
493 system [66]. *E. coli dsbA* mutants activate Cpx [67], which in turn regulates *dsbA* in a feedback
494 loop [68, 69]. In *A. baumannii*, expression of *dsb* genes as well as oxidative stress response
495 genes is modulated by BfmRS [36, 44]. These findings reinforce the view that BfmRS has a
496 subset of activities analogous to those of Cpx [24]. Interestingly, the *E. coli* ortholog of *A.*
497 *baumannii* RnaA, RNase I, is a known DsbA substrate [58], suggesting a potential connection
498 between the two major targets in this study that signal through BfmRS to modulate capsule and
499 Loki susceptibility. RNase I is a non-essential, periplasmic, broad-substrate endonuclease that
500 may serve to catabolize extracellular RNA and generate nucleotide second messengers [59, 70,
501 71]. Unlike RNase I and other RNase T2 family members, *A. baumannii* RnaA lacks key
502 catalytic site residues, making it a probable pseudonuclease. RnaA retains eight cysteines and
503 envelope localization, however, and its levels regulate capsule through BfmRS. A possible
504 interpretation is that *Acinetobacter* has coopted its T2 RNase to function as a sensor of disulfide
505 bond defects and/or oxidative damage in the cell envelope. It is worth noting that a sensor of
506 disulfide bond defects has been reported in *E. coli*, NlpE, which transmits signals to Cpx [67]. *A.*

507 *baumannii* has an NlpE ortholog but it lacks the domain implicated in disulfide sensing [72],
508 suggesting that the pathogen uses a distinct strategy to monitor periplasmic disulfides. Future
509 work will focus on investigating this strategy and defining the connections between RnaA,
510 oxidative folding stress, and BfmS in altering and protecting the *A. baumannii* cell envelope.

511 The LOS outer core is a second cell surface structure that determines vulnerability to
512 Loki attack. Outer core glycosyltransferase mutants producing truncated LOS had increased
513 adsorption and sensitivity to Loki without altered capsule levels. Fully-glycosylated LOS may
514 thus act as a steric barrier decreasing phage binding efficiency. This barrier may impede
515 interactions with membrane-proximal parts of the capsule, or, alternatively, with internal LOS
516 sugars providing a putative secondary receptor, as seen with other phage-bacteria pairs [73].
517 Mutation of *lpxA*, which completely prevents LOS production, was reported to also block Loki
518 adsorption [40]. This could be explained by the loss of the putative secondary receptor, and/or by
519 loss of capsule when early LOS synthesis is blocked [74], although phage susceptibility in total
520 or deeply truncated LOS mutants remain to be examined in depth.

521 While many high-ranking hits in our screen emphasized control of the cell surface in
522 defining sensitivity to phage infection, candidate downstream protective mechanisms were also
523 identified. Deficiency of the Lon protease conferred phage hypersusceptibility without largescale
524 changes to capsule or LOS. This stands in contrast to *lon* mutants in *E. coli*, which show
525 exopolysaccharide overproduction and broad phage resistance [75]. A DNA-modifying
526 methyltransferase, AamA [49], was also identified as a candidate Loki susceptibility
527 determinant. The apparent emphasis of the Tn-seq hits on surface binding vs downstream
528 infection steps may reflect a number of factors, including the importance of the initial cell
529 surface interaction, the screen format focusing on a period of logarithmic bacterial growth, and

530 the particular phage-bacterium pair studied. While intracellular antiviral modules, such as
531 abortive infection or other systems [76], likely affect *A. baumannii*-phage interactions, they are
532 variably present across strains [77] and their existence in ATCC 17978 is uncertain. Additional
533 screens with different phage-bacterial pairs may help expand the known repertoire of
534 susceptibility mechanisms and identify the most conserved elements of intrinsic anti-phage
535 defense in the species.

536 In conclusion, we have analyzed the genome-wide determinants of susceptibility to
537 bacteriophage in *A. baumannii* and identified multiple mechanisms that modulate vulnerability to
538 phage infection, including several linked to altered virulence. Our results expose an Achilles'
539 heel in a pathogenic strategy of *A. baumannii*, capsule hyperproduction, with implications for
540 developing improved antimicrobial therapies involving phage. Future work will examine the
541 mechanisms of cell surface control and the use of combination antimicrobials to manipulate
542 these mechanisms and potentiate killing of the pathogen.

543

544 **Materials and Methods**

545 **Strains and growth conditions.** Bacterial strains used in this work are described in S1 Table. *A.*
546 *baumannii* strains were derivatives of ATCC 17978 unless otherwise noted. Bacteria were
547 cultured in Lysogeny Broth (10 g/L tryptone, 5 g/L yeast extract, 10 g/L NaCl) (LB). Cultures
548 were incubated at 37°C in all cases except phage challenge experiments, which used 30°C unless
549 otherwise indicated. 5mM $CaCl_2$ was added to LB medium in phage challenge experiments.
550 Liquid cultures were aerated with orbital shaking or with rotation via roller drum, with growth
551 monitored by measuring optical density (OD) as absorbance at 600nm ($A_{600}$). LB agar (1.5%
552 w/v) plates were supplemented with antibiotics as needed (tetracycline [Tc] at 10 μg/ml;

553 carbenicillin [Cb] at 50-100 μg/ml, kanamycin [Km] at 10-20 μg/ml, gentamicin [Gm] at 10
554 μg/ml) or sucrose (10% w/v) (Sigma). Isopropyl β-D-thiogalactoside (IPTG) (Sigma) was added
555 to cultures at 0.1-1 mM for induction of P(IPTG)-controlled constructs. Super optimal broth with
556 catabolite repression (SOC) was used in Tn-seq library preparation. Bacteriophage Loki
557 (vB_AbaS_Loki)[40] (gift from Dann Turner) was used in this study.
558
559 **Molecular cloning and strain construction.** Oligonucleotide primers and plasmids used in this
560 study are listed in Table S1. Most sequences were PCR-amplified from the *A. baumannii* 17978
561 genome and cloned in pUC18 before subcloning to destination plasmids. Clones were verified by
562 DNA sequencing (Genewiz/Azenta). Gene deletions were constructed in-frame by allele
563 exchange with cloned ~1kb homology arms using conditionally replicating vectors pSR47S or
564 pJB4648 and sucrose counterselection as described [35]. Deletion mutants were verified by
565 verified by colony PCR. For complementation and overexpression experiments, sequences were
566 subcloned downstream of the *lacI*$^{q}$-T5*lac*P module [P(IPTG)] on plasmid pYDE152. Plasmids
567 were delivered into *A. baumannii* by electroporation.
568
569 **Phage-challenge Tn-seq.** Stocks of *A. baumannii* ATCC 17978 *Mariner* transposon mutants
570 constructed previously [43] were thawed, revived for 1 hour in LB, and then back diluted to
571 OD=0.005 (~$2.5 \times 10^6$ CFU/ml) in LB with 5mM $CaCl_2$ containing Loki or no phage (uninfected
572 control). Cultures were incubated at 37°C to OD ~1 (about 8 doublings). 10 banks of ~20,000
573 mutants per bank were analyzed independently. Two phage treatment arms were used (MOI 1 or
574 1.5, and MOI of 10 or 15). Genomic DNA (gDNA) was extracted (Qiagen DNeasy), quantified
575 by a SYBR green I (Invitrogen) microtiter assay, and tagmented (Illumina Nextera), followed by

576 amplification of transposon-adjacent DNA to form Illumina libraries as described [41, 42].
577 Libraries were size-selected (Pippin HT, 275bp-600bp) and sequenced (single-end 50 bp) using
578 primer mar512 [41] on a HiSeq 2500 with high output V4 chemistry at the Tufts University
579 Genomics Core Facility (TUCF-Genomics).
580 Sequencing read data were processed, mapped to the ATCC 17978 chromosome
581 (NZ_CP012004) and pAB3 (NZ_CP012005), and used to calculate individual transposon mutant
582 fitness based on mutant vs population-wide expansion in each condition using our published
583 pipeline and formula [41]. Fitness values were standardized across conditions by normalizing to
584 the average value of insertions in neutral sites (pseudogenes and endogenous transposon-related
585 genes) within the genome predicted to have no effects on growth. Gene-level average fitness (*W*)
586 was calculated by averaging the fitness values of all individual mutants in a given condition
587 across all pools having a transposon in the first 90% of the gene. Difference in gene-level fitness
588 between phage-challenge and control conditions was deemed significant if it had a magnitude
589 >10%, derived from $n \geq 3$ individual mutants, and had q-value <0.05 in unpaired, two-tailed t
590 test with FDR controlled by the Benjamini, Krieger, and Yekutieli two-stage step-up method
591 (Prism 8). Fitness values at genomic loci were visualized with Integrative Genomics Viewer [78]
592 after aggregation across all transposon mutant libraries via the SingleFitness script [79].
593
594 **Phage-challenge assays.**
595 *i. Liquid infection assay.* Bacterial cultures were diluted to OD=0.003 in LB with 5mM $CaCl_2$
596 and combined with Loki at an MOI=1 or with no phage (uninfected control). Growth was
597 monitored during incubation at 30°C in microtiter plates in an Epoch 2 or Synergy H1M plate
598 reader (Biotek).

599 *ii. Plaque Formation Assay.* Bacterial cultures were diluted to OD=1 in 100µl of LB, combined
600 with 5ml of top agar (LB with 5mM $CaCl_2$ and 0.4% w/v agar), and poured onto LB agar plates.
601 10-fold serial dilutions of phage in Saline-magnesium diluent plus gelatin (SMG) buffer (50mM
602 Tris-HCl, PH=7.5, 100mM NaCl, 8mM MgSO4, 0.01% (W/V) gelatin) [80] were spotted onto
603 the top agar, and plates were incubated at 30°C for 16 hours. Plaques were imaged with white
604 light transillumination using a Chemidoc MP (Bio-Rad).
605 *iii. Phage adsorption assay.* Host bacterial cultures were diluted in LB with 5mM $CaCl_2$ to
606 OD=0.05 and grown at 30°C to OD=0.1. Loki was added at MOI=0.1 followed by incubation at
607 30°C. At regular time intervals, 100 µl were sampled and mixed with 100µl SMG buffer
608 saturated with chloroform. After centrifugation (8000xg, 5 mins), unabsorbed phage within
609 supernatants was enumerated by plaque formation assay. The fraction of free phage was
610 calculated as the number of plaque-forming units (pfu) at each time point divided by the total
611 input pfu.
612
613 **Whole-genome sequencing of spontaneous phage-nonsusceptibility mutants and clinical**
614 **isolates**. Bacterial mutants (derived from *A. baumannii* ATCC 17978 WT or BfmS$^-$) forming
615 colonies within areas of Loki lysis/plaquing were purified on LB agar. gDNA was extracted and
616 quantified as above. Illumina libraries were prepared by a modified Nextera method [36] and
617 sequenced (single-end 100) on a HiSeq 2500 at TUCF-Genomics. Variants were identified from
618 sequencing reads by Breseq as described [81, 82]. Mutations were verified by PCR amplification
619 and Sanger sequencing (Genewiz/Azenta). EGA10 and EGA65 genomes were sequenced and
620 hybrid assembled at SeqCenter using sequencing data from Illumina (NextSeq 2000, 2x151bp)
621 and Oxford Nanopore platforms. The genome assemblies were used for species confirmation and

622 MLST strain type determination (both ST2) [83], and determination of K locus type (both KL22)
623 [84].
624
625 **Capsular polysaccharide analysis.** Capsular polysaccharide was extracted from processed cell
626 lysates and analyzed by alcian blue following described protocols [35]. Samples were collected
627 from early post-exponential phase cultures (OD 2-3) and centrifuged. Cell pellets were
628 resuspended with lysis buffer [60mM Tris, pH 8; 10mM $MgCl_2$; 50µM $CaCl_2$; 20µl/ml DNase
629 (NEB) and RNase cocktail (Amersham); and 3mg/ml lysozyme (Sigma)] and incubated at 37°C
630 for 1 hour. Samples were further processed by 3 liquid nitrogen/37°C freeze-thaw cycles and
631 stepwise treatments with additional DNase and RNase (37°C, 30 minutes), 0.5% SDS (37°C, 30
632 minutes), and Proteinase K (NEB, 60°C, 1 hour). Samples were combined with SDS-PAGE
633 loading buffer, boiled for 5 minutes, and separated on 4-20% Bio-Rad TGX Tris-glycine gels.
634 Capsule was stained with Alcian blue (Sigma), imaged via white light transillumination
635 (ChemiDoc MP), and quantified using Image Lab (Bio-Rad).
636
637 **LOS analysis.** LOS was analyzed via Tricine gel electrophoresis of cell lysates as described
638 [41]. Log phase bacteria were washed with PBS, resuspended with Novex tricine SDS sample
639 buffer (Invitrogen, 50µl 1X buffer per 0.5 OD units of bacteria), and boiled for 15 minutes.
640 Samples were separated on Novex 16% tricine gels (Invitrogen) and stained with Pro-Q Emerald
641 300 (Invitrogen). Gels were imaged using UV transillumination (ChemiDoc MP). Total protein
642 detected with subsequent Coomassie Brilliant Blue staining was used for sample normalization.
643 Relative values were calculated by dividing each normalized LOS value by the total normalized
644 LOS levels in WT [41].

645

646 **Gene expression analysis.** For RT-qPCR, RNA was extracted from log phase bacteria (Qiagen
647 RNeasy), DNase treated (Turbo DNA-free kit, Invitrogen), and reverse transcribed (Superscript
648 II Reverse Transcriptase, Invitrogen). cDNA served as template in qPCR with gene-specific
649 primers (S1 Table) and SYBR Green Master Mix (Applied Biosystems) using a StepOnePlus
650 system according to the manufacturer's instructions. The amplification efficiency for each pair
651 was tested by standard curves using serial diluted cDNA, and found to be > 97% in each case.
652 Fold change in gene expression was calculated by using the $2^{-\Delta\Delta Ct}$ method with *rpoC* as
653 endogenous control [36]. qPCR was performed in technical duplicate from biological triplicate
654 samples. Samples lacking reverse transcriptase were used to confirm absence of signal from
655 residual gDNA. For fluorescence reporter analysis, bacteria were harvested from OD=1 cultures,
656 resuspended in PBS, and transferred to a black, clear bottom microplate (Corning 3631).
657 Fluorescence intensity (excitation at 480 nm/emission at 520 nm) and $A_{600}$ were measured with a
658 Synergy H1M (Biotek). Density-normalized fluorescence units were calculated as fluorescence
659 intensity/$A_{600}$.

660

661 **Analysis of BfmR phosphorylation.** Phosphate affinity electrophoresis was performed
662 following published protocols [85]. 1 OD of mid-log phase bacteria were resuspended in 55µl of
663 BugBuster reagent with 0.1% (v/v) Lysonase (Novagen). Lysis was assisted by repeated
664 pipetting. 18µl of 4X SDS sample buffer (200mM Tris-HCl pH 6.8, 8% SDS, 0.4%
665 Bromophenol blue, 40% Glycerol) was added, and lysates were electrophoresed in Phos-Tag gels
666 (12% acrylamide, 50µM Phos-tag acrylamide, and 100 µM $MnCl_2$) at 30mA. After
667 electrophoresis, gels were incubated for 10 minutes in 1X transfer buffer (50mM Tris, 380mM

668 Glycine, 0.1% SDS, 20% Methanol) with 1mM EDTA to remove manganese, followed by
669 additional 10 minutes in transfer buffer without EDTA. Proteins were transferred to PVDF
670 membranes (100V, 1hr). Total protein was detected in the resulting blots with SYPRO Ruby blot
671 stain (Invitrogen) using the manufacturer's instructions and a GelDoc EZ (Bio-Rad). Blots were
672 incubated in blocking buffer (5% Milk in TBS-T, 1 hour, room temperature) and probed with
673 rabbit anti-BfmR antiserum (1:30,000 or 1:90,000 in blocking buffer, overnight at 4C) and goat
674 anti-rabbit-HRP secondary antibody (Invitrogen, 1:5,000 in blocking buffer, 1 hour at room
675 temperature). Blots were washed 3x10 minutes in TBS-T before and after incubation with
676 secondary antibody, and washed 10min in TBS before developing. Signals were detected with
677 Western Lightning Plus-ECL (Perkin Elmer) and a ChemiDoc MP, and quantified using Image
678 Lab. Rabbit anti-BfmR antiserum was generated by immunizing a rabbit with purified
679 recombinant BfmR according to standard protocols (Pocono Rabbit Farm and Laboratory).
680
681 **Phenotypic signature analysis.** Tn-seq phenotypic signatures belonging to *bfmS*, *rnaA*, and *dsb*
682 paralogs in *A. baumannii* were extracted from previous genome-wide datasets [41]. Hierarchical
683 clustering was performed by the average linkage method using Qlucore Omics Explorer (3.7).
684 Pearson correlation analysis was performed using Prism 9.
685
686 **Microscopy.** Log phase JBA258 bacteria harboring the *rnaA-msGFP2* construct were
687 immobilized on agarose pads (1% in PBS). Fluorescence micrographs were acquired with a
688 100x/1.4 phase-contrast objective on a Zeiss Axio Observer 7 microscope using a 475-nm LED
689 light source (Colibri 7) and filter set 92 HE.
690

691 **Acknowledgements**

692 We thank Dann Turner for the gift of phage Loki; Isabella Bailey, Sarah Hudson, and Wenwen

693 Huo for technical assistance; and members of the Geisinger lab for helpful discussions.

## References


1. Doi Y, Murray GL, Peleg AY. Acinetobacter baumannii: evolution of antimicrobial resistance-treatment options. Semin Respir Crit Care Med. 2015;36(1):85-98. doi: 10.1055/s-0034-1398388. PMID: 25643273.
2. Weiner-Lastinger LM, Abner S, Edwards JR, Kallen AJ, Karlsson M, Magill SS, et al. Antimicrobial-resistant pathogens associated with adult healthcare-associated infections: Summary of data reported to the National Healthcare Safety Network, 2015-2017. Infect Control Hosp Epidemiol. 2019:1-18. Epub 2019/11/27. doi: 10.1017/ice.2019.296. PMID: 31767041.
3. CDC. COVID-19: U.S. Impact on Antimicrobial Resistance, Special Report 2022. Atlanta, GA: U.S. Department of Health and Human Services, CDC, 2022.
4. Rangel K, Chagas TPG, De-Simone SG. Acinetobacter baumannii Infections in Times of COVID-19 Pandemic. Pathogens. 2021;10(8). Epub 2021/08/29. doi: 10.3390/pathogens10081006. PMID: 34451470.
5. Nowak J, Zander E, Stefanik D, Higgins PG, Roca I, Vila J, et al. High incidence of pandrug-resistant Acinetobacter baumannii isolates collected from patients with ventilator-associated pneumonia in Greece, Italy and Spain as part of the MagicBullet clinical trial. J Antimicrob Chemother. 2017;72(12):3277-82. Epub 2017/09/30. doi: 10.1093/jac/dkx322. PMID: 28961773.
6. Qureshi ZA, Hittle LE, O'Hara JA, Rivera JI, Syed A, Shields RK, et al. Colistin-resistant Acinetobacter baumannii: beyond carbapenem resistance. Clin Infect Dis. 2015;60(9):1295-303. Epub 2015/01/30. doi: 10.1093/cid/civ048. PMID: 25632010.
7. Ghaznavi-Rad E, Komijani M, Moradabadi A, Rezaei M, Shaykh-Baygloo N. Isolation of a lytic bacteriophage against extensively drug-resistant Acinetobacter baumannii infections and its dramatic effect in rat model of burn infection. J Clin Lab Anal. 2022;36(7):e24497. Epub 2022/06/17. doi: 10.1002/jcla.24497. PMID: 35708005.
8. Hua Y, Luo T, Yang Y, Dong D, Wang R, Wang Y, et al. Phage Therapy as a Promising New Treatment for Lung Infection Caused by Carbapenem-Resistant Acinetobacter baumannii in Mice. Front Microbiol. 2017;8:2659. Epub 2018/01/30. doi: 10.3389/fmicb.2017.02659. PMID: 29375524.
9. Kusradze I, Karumidze N, Rigvava S, Dvalidze T, Katsitadze M, Amiranashvili I, et al. Characterization and Testing the Efficiency of Acinetobacter baumannii Phage vB-GEC_Ab-M-G7 as an Antibacterial Agent. Front Microbiol. 2016;7:1590. Epub 2016/10/21. doi: 10.3389/fmicb.2016.01590. PMID: 27757110.
10. Wang Y, Mi Z, Niu W, An X, Yuan X, Liu H, et al. Intranasal treatment with bacteriophage rescues mice from Acinetobacter baumannii-mediated pneumonia. Future Microbiol. 2016;11:631-41. Epub 2016/03/02. doi: 10.2217/fmb.16.11. PMID: 26925593.
11. Wu M, Hu K, Xie Y, Liu Y, Mu D, Guo H, et al. A Novel Phage PD-6A3, and Its Endolysin Ply6A3, With Extended Lytic Activity Against Acinetobacter baumannii. Front Microbiol. 2018;9:3302. Epub 2019/01/29. doi: 10.3389/fmicb.2018.03302. PMID: 30687281.
12. Regeimbal JM, Jacobs AC, Corey BW, Henry MS, Thompson MG, Pavlicek RL, et al. Personalized Therapeutic Cocktail of Wild Environmental Phages Rescues Mice from Acinetobacter baumannii Wound Infections. Antimicrob Agents Chemother. 2016;60(10):5806-16. Epub 2016/07/20. doi: 10.1128/AAC.02877-15. PMID: 27431214.
13. Nir-Paz R, Gelman D, Khouri A, Sisson BM, Fackler J, Alkalay-Oren S, et al. Successful Treatment of Antibiotic-resistant, Poly-microbial Bone Infection With Bacteriophages and

740 Antibiotics Combination. Clin Infect Dis. 2019;69(11):2015-8. Epub 2019/03/15. doi:
741 10.1093/cid/ciz222. PMID: 30869755.
742 14. Rao S, Betancourt-Garcia M, Kare-Opaneye YO, Swierczewski BE, Bennett JW, Horne
743 B, et al. Critically Ill Patient with Multidrug-Resistant Acinetobacter baumannii Respiratory
744 Infection Successfully Treated with Intravenous and Nebulized Bacteriophage Therapy.
745 Antimicrob Agents Chemother. 2022;66(1):e0082421. Epub 2021/10/19. doi:
746 10.1128/AAC.00824-21. PMID: 34662188.
747 15. Schooley RT, Biswas B, Gill JJ, Hernandez-Morales A, Lancaster J, Lessor L, et al.
748 Development and Use of Personalized Bacteriophage-Based Therapeutic Cocktails To Treat a
749 Patient with a Disseminated Resistant Acinetobacter baumannii Infection. Antimicrob Agents
750 Chemother. 2017;61(10). Epub 2017/08/16. doi: 10.1128/AAC.00954-17. PMID: 28807909.
751 16. Chen LK, Chang JC, Chu HT, Chen YT, Jiang HL, Wang LS, et al. Preoptimized phage
752 cocktail for use in aerosols against nosocomial transmission of carbapenem-resistant
753 Acinetobacter baumannii: A 3-year prospective intervention study. Ecotoxicol Environ Saf.
754 2022;236:113476. Epub 2022/04/04. doi: 10.1016/j.ecoenv.2022.113476. PMID: 35367880.
755 17. Gordillo Altamirano FL, Barr JJ. Phage Therapy in the Postantibiotic Era. Clin Microbiol
756 Rev. 2019;32(2). Epub 2019/01/18. doi: 10.1128/CMR.00066-18. PMID: 30651225.
757 18. Gordillo Altamirano FL, Kostoulias X, Subedi D, Korneev D, Peleg AY, Barr JJ. Phage-
758 antibiotic combination is a superior treatment against Acinetobacter baumannii in a preclinical
759 study. EBioMedicine. 2022;80:104045. Epub 2022/05/11. doi: 10.1016/j.ebiom.2022.104045.
760 PMID: 35537278.
761 19. Wang X, Loh B, Gordillo Altamirano F, Yu Y, Hua X, Leptihn S. Colistin-phage
762 combinations decrease antibiotic resistance in Acinetobacter baumannii via changes in envelope
763 architecture. Emerg Microbes Infect. 2021;10(1):2205-19. Epub 2021/11/06. doi:
764 10.1080/22221751.2021.2002671. PMID: 34736365.
765 20. Abdelkader K, Gutierrez D, Latka A, Boeckaerts D, Drulis-Kawa Z, Criel B, et al. The
766 Specific Capsule Depolymerase of Phage PMK34 Sensitizes Acinetobacter baumannii to Serum
767 Killing. Antibiotics (Basel). 2022;11(5). Epub 2022/05/29. doi: 10.3390/antibiotics11050677.
768 PMID: 35625321.
769 21. Gordillo Altamirano F, Forsyth JH, Patwa R, Kostoulias X, Trim M, Subedi D, et al.
770 Bacteriophage-resistant Acinetobacter baumannii are resensitized to antimicrobials. Nat
771 Microbiol. 2021;6(2):157-61. Epub 2021/01/13. doi: 10.1038/s41564-020-00830-7. PMID:
772 33432151.
773 22. Popova AV, Shneider MM, Arbatsky NP, Kasimova AA, Senchenkova SN, Shashkov
774 AS, et al. Specific Interaction of Novel Friunavirus Phages Encoding Tailspike Depolymerases
775 with Corresponding Acinetobacter baumannii Capsular Types. J Virol. 2020. Epub 2020/12/04.
776 doi: 10.1128/JVI.01714-20. PMID: 33268523.
777 23. Liu M, Hernandez-Morales A, Clark J, Le T, Biswas B, Bishop-Lilly KA, et al.
778 Comparative genomics of Acinetobacter baumannii and therapeutic bacteriophages from a
779 patient undergoing phage therapy. Nat Commun. 2022;13(1):3776. Epub 2022/07/01. doi:
780 10.1038/s41467-022-31455-5. PMID: 35773283.
781 24. Geisinger E, Huo W, Hernandez-Bird J, Isberg RR. Acinetobacter baumannii: Envelope
782 Determinants That Control Drug Resistance, Virulence, and Surface Variability. Annu Rev
783 Microbiol. 2019;73:481-506. Epub 2019/06/18. doi: 10.1146/annurev-micro-020518-115714.
784 PMID: 31206345.

785 25. Oliveira H, Mendes A, Fraga AG, Ferreira A, Pimenta AI, Mil-Homens D, et al. K2
786 Capsule Depolymerase Is Highly Stable, Is Refractory to Resistance, and Protects Larvae and
787 Mice from Acinetobacter baumannii Sepsis. Appl Environ Microbiol. 2019;85(17). Epub
788 2019/06/23. doi: 10.1128/AEM.00934-19. PMID: 31227554.
789 26. Talyansky Y, Nielsen TB, Yan J, Carlino-Macdonald U, Di Venanzio G, Chakravorty S,
790 et al. Capsule carbohydrate structure determines virulence in Acinetobacter baumannii. PLoS
791 Pathog. 2021;17(2):e1009291. Epub 2021/02/03. doi: 10.1371/journal.ppat.1009291. PMID:
792 33529209.
793 27. Giguere D. Surface polysaccharides from Acinetobacter baumannii: Structures and
794 syntheses. Carbohydr Res. 2015;418:29-43. Epub 2015/11/05. doi: 10.1016/j.carres.2015.10.001.
795 PMID: 26531136.
796 28. Koeleman JG, van der Bijl MW, Stoof J, Vandenbroucke-Grauls CM, Savelkoul PH.
797 Antibiotic resistance is a major risk factor for epidemic behavior of Acinetobacter baumannii.
798 Infect Control Hosp Epidemiol. 2001;22(5):284-8. Epub 2001/06/29. doi: ICHE6806 [pii]
799 10.1086/501901. PMID: 11428438.
800 29. Kenyon JJ, Hall RM. Variation in the complex carbohydrate biosynthesis loci of
801 Acinetobacter baumannii genomes. PLoS One. 2013;8(4):e62160. Epub 2013/04/25. doi:
802 10.1371/journal.pone.0062160. PMID: 23614028.
803 30. Kenyon JJ, Hall RM. Updated Analysis of the Surface Carbohydrate Gene Clusters in a
804 Diverse Panel of Acinetobacter baumannii Isolates. Antimicrob Agents Chemother.
805 2022;66(1):e0180721. Epub 2021/10/19. doi: 10.1128/AAC.01807-21. PMID: 34662195.
806 31. Shashkov AS, Kenyon JJ, Senchenkova SN, Shneider MM, Popova AV, Arbatsky NP, et
807 al. Acinetobacter baumannii K27 and K44 capsular polysaccharides have the same K unit but
808 different structures due to the presence of distinct wzy genes in otherwise closely related K gene
809 clusters. Glycobiology. 2016;26(5):501-8. Epub 2015/12/30. doi: 10.1093/glycob/cwv168.
810 PMID: 26711304.
811 32. Huang X, Li X, An H, Wang J, Ding M, Wang L, et al. Capsule type defines the
812 capability of Klebsiella pneumoniae in evading Kupffer cell capture in the liver. PLoS Pathog.
813 2022;18(8):e1010693. Epub 2022/08/02. doi: 10.1371/journal.ppat.1010693. PMID: 35914009.
814 33. Hathaway LJ, Grandgirard D, Valente LG, Tauber MG, Leib SL. Streptococcus
815 pneumoniae capsule determines disease severity in experimental pneumococcal meningitis. Open
816 Biol. 2016;6(3). Epub 2016/03/25. doi: 10.1098/rsob.150269. PMID: 27009189.
817 34. Melin M, Trzcinski K, Meri S, Kayhty H, Vakevainen M. The capsular serotype of
818 Streptococcus pneumoniae is more important than the genetic background for resistance to
819 complement. Infect Immun. 2010;78(12):5262-70. Epub 2010/09/22. doi: 10.1128/IAI.00740-10.
820 PMID: 20855513.
821 35. Geisinger E, Isberg RR. Antibiotic modulation of capsular exopolysaccharide and
822 virulence in Acinetobacter baumannii. PLoS Pathog. 2015;11(2):e1004691. Epub 2015/02/14.
823 doi: 10.1371/journal.ppat.1004691. PMID: 25679516.
824 36. Geisinger E, Mortman NJ, Vargas-Cuebas G, Tai AK, Isberg RR. A global regulatory
825 system links virulence and antibiotic resistance to envelope homeostasis in Acinetobacter
826 baumannii. PLoS Pathog. 2018;14(5):e1007030. Epub 2018/05/26. doi:
827 10.1371/journal.ppat.1007030. PMID: 29795704.
828 37. Chin CY, Tipton KA, Farokhyfar M, Burd EM, Weiss DS, Rather PN. A high-frequency
829 phenotypic switch links bacterial virulence and environmental survival in Acinetobacter

830 baumannii. Nat Microbiol. 2018;3(5):563-9. Epub 2018/04/26. doi: 10.1038/s41564-018-0151-5.
831 PMID: 29693659.
832 38. Tierney ARP, Chin CY, Weiss DS, Rather PN. A LysR-Type Transcriptional Regulator
833 Controls Multiple Phenotypes in Acinetobacter baumannii. Front Cell Infect Microbiol.
834 2021;11:778331. Epub 2021/11/23. doi: 10.3389/fcimb.2021.778331. PMID: 34805000.
835 39. Tipton KA, Chin CY, Farokhyfar M, Weiss DS, Rather PN. Role of Capsule in
836 Resistance to Disinfectants, Host Antimicrobials, and Desiccation in Acinetobacter baumannii.
837 Antimicrob Agents Chemother. 2018;62(12). Epub 2018/10/10. doi: 10.1128/AAC.01188-18.
838 PMID: 30297362.
839 40. Turner D, Wand ME, Briers Y, Lavigne R, Sutton JM, Reynolds DM. Characterisation
840 and genome sequence of the lytic Acinetobacter baumannii bacteriophage vB_AbaS_Loki. PLoS
841 One. 2017;12(2):e0172303. Epub 2017/02/17. doi: 10.1371/journal.pone.0172303. PMID:
842 28207864.
843 41. Geisinger E, Mortman NJ, Dai Y, Cokol M, Syal S, Farinha A, et al. Antibiotic
844 susceptibility signatures identify potential antimicrobial targets in the Acinetobacter baumannii
845 cell envelope. Nature Communications. 2020;11(1):4522. doi: 10.1038/s41467-020-18301-2.
846 42. Geisinger E, Vargas-Cuebas G, Mortman NJ, Syal S, Dai Y, Wainwright EL, et al. The
847 Landscape of Phenotypic and Transcriptional Responses to Ciprofloxacin in Acinetobacter
848 baumannii: Acquired Resistance Alleles Modulate Drug-Induced SOS Response and Prophage
849 Replication. MBio. 2019;10(3). Epub 2019/06/13. doi: 10.1128/mBio.01127-19. PMID:
850 31186328.
851 43. Bai J, Dai Y, Farinha A, Tang AY, Syal S, Vargas-Cuebas G, et al. Essential gene
852 analysis in Acinetobacter baumannii by high-density transposon mutagenesis and CRISPR
853 interference. J Bacteriol. 2021;203(12). Epub 2021/03/31. doi: 10.1128/JB.00565-20. PMID:
854 33782056.
855 44. Palethorpe S, Farrow JM, 3rd, Wells G, Milton ME, Actis LA, Cavanagh J, et al.
856 Acinetobacter baumannii Regulates Its Stress Responses via the BfmRS Two-Component
857 Regulatory System. J Bacteriol. 2022;204(2):e0049421. Epub 2021/12/07. doi:
858 10.1128/JB.00494-21. PMID: 34871031.
859 45. Premkumar L, Kurth F, Duprez W, Groftehauge MK, King GJ, Halili MA, et al.
860 Structure of the Acinetobacter baumannii dithiol oxidase DsbA bound to elongation factor EF-Tu
861 reveals a novel protein interaction site. J Biol Chem. 2014;289(29):19869-80. Epub 2014/05/27.
862 doi: 10.1074/jbc.M114.571737. PMID: 24860094.
863 46. Landeta C, Boyd D, Beckwith J. Disulfide bond formation in prokaryotes. Nat Microbiol.
864 2018;3(3):270-80. Epub 2018/02/22. doi: 10.1038/s41564-017-0106-2. PMID: 29463925.
865 47. Cech GM, Kloska A, Krause K, Potrykus K, Cashel M, Szalewska-Palasz A. Virus-Host
866 Interaction Gets Curiouser and Curiouser. PART I: Phage P1vir Enhanced Development in an E.
867 coli DksA-Deficient Cell. Int J Mol Sci. 2021;22(11). Epub 2021/06/03. doi:
868 10.3390/ijms22115890. PMID: 34072628.
869 48. Patterson-West J, James TD, Fernandez-Coll L, Iben JR, Moon K, Knipling L, et al. The
870 E. coli Global Regulator DksA Reduces Transcription during T4 Infection. Viruses. 2018;10(6).
871 Epub 2018/06/09. doi: 10.3390/v10060308. PMID: 29882792.
872 49. Blaschke U, Suwono B, Zafari S, Ebersberger I, Skiebe E, Jeffries CM, et al.
873 Recombinant production of A1S_0222 from Acinetobacter baumannii ATCC 17978 and
874 confirmation of its DNA-(adenine N6)-methyltransferase activity. Protein Expr Purif.
875 2018;151:78-85. Epub 2018/06/18. doi: 10.1016/j.pep.2018.06.009. PMID: 29908915.

876 50. Harding CM, Haurat MF, Vinogradov E, Feldman MF. Distinct amino acid residues
877 confer one of three UDP-sugar substrate specificities in Acinetobacter baumannii PglC
878 phosphoglycosyltransferases. Glycobiology. 2018;28(7):522-33. Epub 2018/04/19. doi:
879 10.1093/glycob/cwy037. PMID: 29668902.
880 51. Tickner J, Hawas S, Totsika M, Kenyon JJ. The Wzi outer membrane protein mediates
881 assembly of a tight capsular polysaccharide layer on the Acinetobacter baumannii cell surface.
882 Sci Rep. 2021;11(1):21741. Epub 2021/11/07. doi: 10.1038/s41598-021-01206-5. PMID:
883 34741090.
884 52. Lees-Miller RG, Iwashkiw JA, Scott NE, Seper A, Vinogradov E, Schild S, et al. A
885 common pathway for O-linked protein-glycosylation and synthesis of capsule in Acinetobacter
886 baumannii. Mol Microbiol. 2013;89(5):816-30. Epub 2013/06/21. doi: 10.1111/mmi.12300.
887 PMID: 23782391.
888 53. Hamidian M, Blasco L, Tillman LN, To J, Tomas M, Myers GSA. Analysis of Complete
889 Genome Sequence of Acinetobacter baumannii Strain ATCC 19606 Reveals Novel Mobile
890 Genetic Elements and Novel Prophage. Microorganisms. 2020;8(12). Epub 2020/12/02. doi:
891 10.3390/microorganisms8121851. PMID: 33255319.
892 54. Senchenkova SN, Shashkov AS, Popova AV, Shneider MM, Arbatsky NP, Miroshnikov
893 KA, et al. Structure elucidation of the capsular polysaccharide of Acinetobacter baumannii
894 AB5075 having the KL25 capsule biosynthesis locus. Carbohydr Res. 2015;408:8-11. Epub
895 2015/03/31. doi: 10.1016/j.carres.2015.02.011. PMID: 25816997.
896 55. Draughn GL, Milton ME, Feldmann EA, Bobay BG, Roth BM, Olson AL, et al. The
897 Structure of the Biofilm-controlling Response Regulator BfmR from Acinetobacter baumannii
898 Reveals Details of Its DNA-binding Mechanism. J Mol Biol. 2018;430(6):806-21. Epub
899 2018/02/14. doi: 10.1016/j.jmb.2018.02.002. PMID: 29438671.
900 56. Russo TA, Manohar A, Beanan JM, Olson R, MacDonald U, Graham J, et al. The
901 Response Regulator BfmR Is a Potential Drug Target for Acinetobacter baumannii. mSphere.
902 2016;1(3). doi: 10.1128/mSphere.00082-16. PMID: 27303741.
903 57. Ganguli S, Wang H, Matsumura P, Volz K. Uncoupled phosphorylation and activation in
904 bacterial chemotaxis. The 2.1-A structure of a threonine to isoleucine mutant at position 87 of
905 CheY. J Biol Chem. 1995;270(29):17386-93. Epub 1995/07/21. PMID: 7615544.
906 58. Messens J, Collet JF, Van Belle K, Brosens E, Loris R, Wyns L. The oxidase DsbA folds
907 a protein with a nonconsecutive disulfide. J Biol Chem. 2007;282(43):31302-7. Epub
908 2007/08/19. doi: 10.1074/jbc.M705236200. PMID: 17702751.
909 59. Deshpande RA, Shankar V. Ribonucleases from T2 family. Crit Rev Microbiol.
910 2002;28(2):79-122. Epub 2002/07/12. doi: 10.1080/1040-840291046704. PMID: 12109772.
911 60. Jacobs AC, Blanchard CE, Catherman SC, Dunman PM, Murata Y. An ribonuclease T2
912 family protein modulates Acinetobacter baumannii abiotic surface colonization. PLoS One.
913 2014;9(1):e85729. Epub 2014/02/04. doi: 10.1371/journal.pone.0085729. PMID: 24489668.
914 61. Ching C, Yang B, Onwubueke C, Lazinski D, Camilli A, Godoy VG. Lon Protease Has
915 Multifaceted Biological Functions in Acinetobacter baumannii. J Bacteriol. 2019;201(2). Epub
916 2018/10/24. doi: 10.1128/JB.00536-18. PMID: 30348832.
917 62. Gordillo Altamirano FL, Barr JJ. Unlocking the next generation of phage therapy: the key
918 is in the receptors. Curr Opin Biotechnol. 2021;68:115-23. Epub 2020/11/18. doi:
919 10.1016/j.copbio.2020.10.002. PMID: 33202354.

920 63. Knezevic P, Curcin S, Aleksic V, Petrusic M, Vlaski L. Phage-antibiotic synergism: a
921 possible approach to combatting Pseudomonas aeruginosa. Res Microbiol. 2013;164(1):55-60.
922 Epub 2012/09/25. doi: 10.1016/j.resmic.2012.08.008. PMID: 23000091.
923 64. Luo J, Xie L, Liu M, Li Q, Wang P, Luo C. Bactericidal Synergism between Phage
924 YC#06 and Antibiotics: a Combination Strategy to Target Multidrug-Resistant Acinetobacter
925 baumannii In Vitro and In Vivo. Microbiol Spectr. 2022:e0009622. Epub 2022/06/24. doi:
926 10.1128/spectrum.00096-22. PMID: 35736241.
927 65. Furniss RCD, Kaderabkova N, Barker D, Bernal P, Maslova E, Antwi AAA, et al.
928 Breaking antimicrobial resistance by disrupting extracytoplasmic protein folding. Elife. 2022;11.
929 Epub 2022/01/14. doi: 10.7554/eLife.57974. PMID: 35025730.
930 66. Collet JF, Cho SH, Iorga BI, Goemans CV. How the assembly and protection of the
931 bacterial cell envelope depend on cysteine residues. J Biol Chem. 2020;295(34):11984-94. Epub
932 2020/06/04. doi: 10.1074/jbc.REV120.011201. PMID: 32487747.
933 67. Delhaye A, Laloux G, Collet JF. The Lipoprotein NlpE Is a Cpx Sensor That Serves as a
934 Sentinel for Protein Sorting and Folding Defects in the Escherichia coli Envelope. J Bacteriol.
935 2019;201(10). Epub 2019/03/06. doi: 10.1128/JB.00611-18. PMID: 30833359.
936 68. Danese PN, Silhavy TJ. The sigma(E) and the Cpx signal transduction systems control
937 the synthesis of periplasmic protein-folding enzymes in Escherichia coli. Genes Dev.
938 1997;11(9):1183-93. Epub 1997/05/01. doi: 10.1101/gad.11.9.1183. PMID: 9159399.
939 69. Pogliano J, Lynch AS, Belin D, Lin EC, Beckwith J. Regulation of Escherichia coli cell
940 envelope proteins involved in protein folding and degradation by the Cpx two-component
941 system. Genes Dev. 1997;11(9):1169-82. Epub 1997/05/01. doi: 10.1101/gad.11.9.1169. PMID:
942 9159398.
943 70. Duggal Y, Fontaine BM, Dailey DM, Ning G, Weinert EE. RNase I Modulates
944 Escherichia coli Motility, Metabolism, and Resistance. ACS Chem Biol. 2020;15(7):1996-2004.
945 Epub 2020/06/20. doi: 10.1021/acschembio.0c00390. PMID: 32551492.
946 71. Fontaine BM, Martin KS, Garcia-Rodriguez JM, Jung C, Briggs L, Southwell JE, et al.
947 RNase I regulates Escherichia coli 2',3'-cyclic nucleotide monophosphate levels and biofilm
948 formation. Biochem J. 2018;475(8):1491-506. Epub 2018/03/21. doi: 10.1042/BCJ20170906.
949 PMID: 29555843.
950 72. Hirano Y, Hossain MM, Takeda K, Tokuda H, Miki K. Structural studies of the Cpx
951 pathway activator NlpE on the outer membrane of Escherichia coli. Structure. 2007;15(8):963-
952 76. Epub 2007/08/19. doi: 10.1016/j.str.2007.06.014. PMID: 17698001.
953 73. Gong Q, Wang X, Huang H, Sun Y, Qian X, Xue F, et al. Novel Host Recognition
954 Mechanism of the K1 Capsule-Specific Phage of Escherichia coli: Capsular Polysaccharide as
955 the First Receptor and Lipopolysaccharide as the Secondary Receptor. J Virol.
956 2021;95(18):e0092021. Epub 2021/07/01. doi: 10.1128/JVI.00920-21. PMID: 34191582.
957 74. Zhang G, Baidin V, Pahil KS, Moison E, Tomasek D, Ramadoss NS, et al. Cell-based
958 screen for discovering lipopolysaccharide biogenesis inhibitors. Proc Natl Acad Sci U S A.
959 2018;115(26):6834-9. Epub 2018/05/08. doi: 10.1073/pnas.1804670115. PMID: 29735709.
960 75. Kortright KE, Chan BK, Turner PE. High-throughput discovery of phage receptors using
961 transposon insertion sequencing of bacteria. Proc Natl Acad Sci U S A. 2020;117(31):18670-9.
962 Epub 2020/07/18. doi: 10.1073/pnas.2001888117. PMID: 32675236.
963 76. Bernheim A, Sorek R. The pan-immune system of bacteria: antiviral defence as a
964 community resource. Nat Rev Microbiol. 2020;18(2):113-9. Epub 2019/11/07. doi:
965 10.1038/s41579-019-0278-2. PMID: 31695182.

966 77. Ambroa A, Blasco L, Lopez M, Pacios O, Bleriot I, Fernandez-Garcia L, et al. Genomic
967 Analysis of Molecular Bacterial Mechanisms of Resistance to Phage Infection. Front Microbiol.
968 2021;12:784949. Epub 2022/03/08. doi: 10.3389/fmicb.2021.784949. PMID: 35250902.
969 78. Robinson JT, Thorvaldsdottir H, Winckler W, Guttman M, Lander ES, Getz G, et al.
970 Integrative genomics viewer. Nat Biotechnol. 2011;29(1):24-6. Epub 2011/01/12. doi:
971 10.1038/nbt.1754. PMID: 21221095.
972 79. McCoy KM, Antonio ML, van Opijnen T. MAGenTA: a Galaxy implemented tool for
973 complete Tn-Seq analysis and data visualization. Bioinformatics. 2017;33(17):2781-3. Epub
974 2017/05/13. doi: 10.1093/bioinformatics/btx320. PMID: 28498899.
975 80. Kropinski AM, Mazzocco A, Waddell TE, Lingohr E, Johnson RP. Enumeration of
976 bacteriophages by double agar overlay plaque assay. Methods Mol Biol. 2009;501:69-76. Epub
977 2008/12/11. doi: 10.1007/978-1-60327-164-6_7. PMID: 19066811.
978 81. Dai Y, Pinedo V, Tang AY, Cava F, Geisinger E. A New Class of Cell Wall-Recycling
979 l,d-Carboxypeptidase Determines beta-Lactam Susceptibility and Morphogenesis in
980 Acinetobacter baumannii. mBio. 2021;12(6):e0278621. Epub 2021/12/08. doi:
981 10.1128/mBio.02786-21. PMID: 34872350.
982 82. Deatherage DE, Barrick JE. Identification of mutations in laboratory-evolved microbes
983 from next-generation sequencing data using breseq. Methods Mol Biol. 2014;1151:165-88. doi:
984 10.1007/978-1-4939-0554-6_12. PMID: 24838886.
985 83. Jolley KA, Bray JE, Maiden MCJ. Open-access bacterial population genomics: BIGSdb
986 software, the PubMLST.org website and their applications. Wellcome Open Res. 2018;3:124.
987 Epub 2018/10/23. doi: 10.12688/wellcomeopenres.14826.1. PMID: 30345391.
988 84. Wyres KL, Cahill SM, Holt KE, Hall RM, Kenyon JJ. Identification of Acinetobacter
989 baumannii loci for capsular polysaccharide (KL) and lipooligosaccharide outer core (OCL)
990 synthesis in genome assemblies using curated reference databases compatible with Kaptive.
991 Microb Genom. 2020;6(3). Epub 2020/03/03. doi: 10.1099/mgen.0.000339. PMID: 32118530.
992 85. Gao R, Stock AM. Probing kinase and phosphatase activities of two-component systems
993 in vivo with concentration-dependent phosphorylation profiling. Proc Natl Acad Sci U S A.
994 2013;110(2):672-7. Epub 2012/12/26. doi: 10.1073/pnas.1214587110. PMID: 23267085.
995 86. Marchler-Bauer A, Bo Y, Han L, He J, Lanczycki CJ, Lu S, et al. CDD/SPARCLE:
996 functional classification of proteins via subfamily domain architectures. Nucleic Acids Res.
997 2017;45(D1):D200-D3. Epub 2016/12/03. doi: 10.1093/nar/gkw1129. PMID: 27899674.
998 87. Almagro Armenteros JJ, Tsirigos KD, Sonderby CK, Petersen TN, Winther O, Brunak S,
999 et al. SignalP 5.0 improves signal peptide predictions using deep neural networks. Nat
1000 Biotechnol. 2019;37(4):420-3. Epub 2019/02/20. doi: 10.1038/s41587-019-0036-z. PMID:
1001 30778233.
1002

1003 **Captions**

1004 **Fig 1. Identification of candidate determinants of susceptibility to Loki using Tn-seq.**

1005 (A) Loki infection of *A. baumannii* ATCC 17978 causes partial inhibition of bulk culture growth.
1006 Bacteria were seeded in microplates with or without Loki at the indicated MOI and growth was
1007 monitored by OD readings (liquid infection assay). Data points show geometric mean ± s.d.
1008 (shaded bands) from n = 3 independent cultures. Where not visible, s.d. is within the confines of
1009 the symbol. Inset shows small, turbid plaques resulting from Loki infection of ATCC 17978 on
1010 solid medium. Plaques imaged with white light transillumination. Scale bar, 1 mm. (B) Tn-seq
1011 analysis of Loki susceptibility determinants in *A. baumannii* ATCC 17978. Volcano plots show
1012 change in gene-level fitness resulting from phage treatment at the indicated MOI compared to
1013 untreated control, plotted against inverse p value from parallel t tests. Blue data points are genes
1014 that pass significance criteria (Materials and Methods) and represent candidate Loki
1015 susceptibility determinants. Loci described further in the text are labelled. Grey data points are
1016 genes not passing significance criteria.

1017

1018 **Fig 2. Validation of candidate phage hypersusceptibility loci.**

1019 (A) Tracks show Tn-seq fitness values (vertical bars) of individual *Mariner* transposon mutants
1020 at candidate Loki hypersusceptibility loci (shaded yellow) across all tested mutant banks using
1021 the indicated MOI. With the *slt-rnaA* locus, insertions with major fitness decrease due to Loki
1022 show bias toward *rnaA* and the 3' end of *slt*. (B-D) Liquid infection assays with defined mutants.
1023 Growth of the indicated *A. baumannii* ATCC 17978 strains with (Loki, MOI 1) or without
1024 (uninf.) phage was measured as in Fig 1A (n=3). "Chr" indicates the chromosomal mutation;
1025 "Plasmid" denotes the gene reintroduced under P(IPTG) control via vector pYDE152, with -

1026 indicating control plasmid with no reintroduced gene; *bfmS** refers to BfmS$^-$ point mutant
1027 EGA127; IPTG "0.1" and "1" refer to mM units. (E-F) Plaque formation assays. ~$10^8$ of the
1028 indicated bacteria were overlaid on bottom agar, followed by spotting 10-fold serial dilutions of
1029 Loki. Bottom agar in E contained 1mM IPTG. Plaques were imaged with white-light
1030 transillumination after 16 h incubation at 30°C.
1031
1032 **Fig 3. Loki resistance mutations map to capsule biosynthesis locus.** (A) Tn-seq fitness of
1033 transposon mutants in the capsule synthesis (KL3) and associated loci in the Loki challenge
1034 screen. Plotted are the average gene-level Tn-seq fitness values (*W*) with phage infection (Loki
1035 MOI 10-15) vs uninfected control, analyzed by unpaired t-tests. X indicates essential gene
1036 without a fitness value due to paucity of transposon insertions. Dotted line indicates the genome-
1037 wide average *W* during Loki challenge. (B-C) Plaque formation assays with Loki spotted on
1038 acapsular *itrA* and *wzc* mutants of ATCC 17978 (B) or on a range of *A. baumannii* clinical
1039 isolates (C) showing dependence on the KL3 capsule for infection. Δ*itrA* P(IPTG)-*itrA*
1040 represents Δ*itrA* harboring pJE172 and was grown with the indicated concentration of IPTG in
1041 bottom agar. (D) Diagram of the KL3/KL22 cluster showing spontaneous Loki resistance
1042 mutations (arrowheads). The hotspot within *gtr6* is expanded. KL3 and KL22 share all ORFs
1043 except *pgt1* (only present in KL22). (E-F) Plaque formation assays with Loki spotted on strains
1044 with spontaneous *gtr6* mutations and the indicated pYDE152-based plasmid (E) or with *gtr6*
1045 deletion (F). Bottom agar in E contained 1mM IPTG. (G) Phage adsorption assay measuring
1046 Loki binding to the acapsular Δ*itrA* and Δ*wzc* mutants and altered capsule *gtr6* mutants. Data
1047 points show geometric mean ± s.d. (n=3), analyzed by unpaired t test (capsule mutant vs WT
1048 control). P values: *, ≤0.05; **, ≤0.01; ***, <0.001.

1049

1050 **Fig 4. Susceptibility to Loki depends on BfmRS activity and correlates with control of**

1051 **capsule levels.**

1052 (A) Tn-seq fitness of *bfmS* and *bfmR* transposon mutants in the phage challenge screen. Data

1053 points show average gene-level Tn-seq fitness values (*W*) with Loki infection at indicated MOI

1054 vs uninfected control, analyzed by unpaired t-tests. Dotted line indicates the genome-wide

1055 average *W* during Loki challenge (MOI 10-15). (B) Capsule production by different *bfmRS*

1056 mutants. Bars show mean capsule level ± s.d. (n=3), analyzed by one-way ANOVA with

1057 Dunnett's multiple comparisons test (mutant vs WT). A representative gel is shown above the

1058 graph. (C) Liquid infection and (D, E) plaque formation assays with Δ*bfmRS* and *bfmR* receiver

1059 domain point mutants. Liquid infection assays used an MOI of 1, and data are presented as in Fig

1060 1A (n=3). (F) BfmR phosphorylation level was analyzed in cell lysates of receiver domain

1061 mutants vs the parent control (*bfmS**) by Phos-tag western blotting. BfmR~P as a fraction of

1062 total BfmR was quantified from n=3 samples. Bars show mean ± s.d., analyzed by one-way

1063 ANOVA with Tukey's multiple comparisons test. A representative blot is shown above the

1064 graph. (G) Phage adsorption assay showing opposing effects of *bfmS** and Δ*bfmRS* mutations on

1065 Loki binding, analyzed as in Fig 3G (n=3). *bfmS** refers to BfmS$^-$ point mutant EGA127. P

1066 values: *, ≤0.05; **, ≤0.01; ***, <0.001.

1067

1068 **Fig 5. RnaA and DsbA modulate capsule production and Loki susceptibility through**

1069 **BfmRS.**

1070 (A) Capsule levels measured in strains with Δ*rnaA* and Δ*dsbA* mutation singly and in

1071 combination with Δ*bfmRS*. A representative gel (top) and quantification from n=3 samples

1072 (bottom; means ± s.d. analyzed by one-way ANOVA with Šídák's multiple comparisons test) are
1073 shown as in Fig 4B. (B) Phage adsorption assays show increased Loki binding to *rnaA* and *dsbA*
1074 mutants. Assays analyzed as in Fig 3G (n=3). (C) Transcription levels of capsule biosynthesis
1075 genes *wza* and *gnaA* measured by qRT-PCR in Δ*rnaA* and Δ*dsbA* mutants. Bars show mean fold
1076 change vs WT ± s.d. (n=3); analyzed by unpaired t-tests comparing each mutant vs WT. (D)
1077 Liquid infection and (E) plaque assays examining susceptibility of strains in A to Loki attack.
1078 Liquid growth data presented as in Fig 1A (n=6.). (F-G) *rnaA* overexpression via high-copy
1079 plasmid decreases capsule production and blocks Loki infection in a manner dependent on the
1080 BfmS signal receptor. WT ($BfmS^+$) or *bfmS** ($BfmS^-$) bacteria harbored pJE127 (IPTG-
1081 dependent *rnaA*) and were grown in the presence or absence of IPTG. Representative capsule gel
1082 (F, top), capsule quantification from n=3 samples (F, bottom), and Loki plaque assays (G) are
1083 shown. Mean capsule levels ± s.d. were analyzed by unpaired t-tests. P values: *, ≤0.05; **,
1084 ≤0.01; ***, <0.001. ns, not significant.
1085
1086 **Fig 6. RnaA/DsbA deficiency activates BfmRS.**
1087 (A-B) Fluorescence reporter assays. Strains harbored a GFP transcriptional fusion to the noted
1088 promoter region and reporter fluorescence was measured as fluorescence units/$A_{600}$. (A) Δ*rnaA*
1089 and Δ*dsbA* activation of a BfmRS-dependent (*18040*p), but not BfmRS-independent (*adc*p)
1090 promoter. (B) Δ*rnaA*/Δ*dsbA* activation of *18040*p requires BfmRS. Bars show mean ± s.d. (n =
1091 3). Means were analyzed by unpaired t test comparing mutant vs WT (A) or by one-way
1092 ANOVA with Šídák's multiple comparisons test (B). (C) Phos-tag analysis of BfmR
1093 phosphorylation levels. Δ*rnaA* and Δ*dsbA* increase BfmR~P to a level matching that caused by
1094 the hyperactive Δ*bfmS* allele. Presented as in Fig 4F (n=3). Asterisks show results of one-way

1095 ANOVA with Tukey's multiple comparisons test (mutant vs WT); comparisons between mutants
1096 were not significant. (D) Heat map shows the Pearson correlation coefficients (r) and associated
1097 P values analyzing relatedness of Tn-seq phenotypic signatures [41] of *bfmS, rnaA,* and *dsb*
1098 genes. (E) Tn-seq fitness of *rnaA* and *dsb* transposon mutants in the phage challenge screen.
1099 Data presented as in Fig 4A. (F) Δ*dsbA* but not Δ*rnaA* shows a synthetic growth defect with
1100 Δ*bfmRS.* Bacteria were incubated in LB at 37°C and growth measured as in Fig 1A (n=3). P
1101 values: *, ≤0.05; **, ≤0.01; ***, <0.001. ns, not significant.
1102
1103 **Fig 7. *A. baumannii* RnaA lacks catalytic residues defining the RNase T2 family and shows**
1104 **cell envelope localization.**
1105 (A) Analysis of conserved domains on RnaA. RNase_T2 domain and conserved Features/Sites
1106 were identified using the NCBI Conserved Domain Database [86]. Signal peptide was identified
1107 using SignalP [87]. Vertical green lines represent conserved cysteine residues within the
1108 RNase_T2 domain. Alignment shows RNase T2 family homologs across diverse bacterial
1109 species. Within the conserved active site motifs (CAS-I and CAS-II), the active sites are
1110 indicated by #, and the most commonly found residues at these sites are highlighted. (B) An
1111 RnaA-msGFP2 fusion produces foci localized to the cell periphery, consistent with predicted
1112 secretion to periplasm. Δ*rnaA* cells harboring the fusion protein were imaged by fluorescence
1113 microscopy. Scale bar, 2.5 µm. (C) A cell magnified 2.5X; scale bar, 1 µm.
1114
1115 **Fig 8. The full-length LOS outer core impedes attack by Loki independent of changes to**
1116 **capsule.**

1117 (A-B) Representative LOS gels (A) and quantification from triplicate samples (B) showing
1118 enrichment of a truncated LOS intermediate in Δ*gtrOC3* and Δ*gtrOC4*. Bars in B show mean
1119 normalized LOS levels ± s.d.; one-way ANOVA showed no significant difference in total LOS
1120 levels among strains (P=0.34). (C-D) Δ*gtrOC3* and Δ*gtrOC4* have no effect on capsule levels.
1121 Capsule analyzed as in Fig 4B (n=3; P=0.96, one-way ANOVA). (E) Tn-seq fitness of LOS
1122 outer core synthesis locus (OCL2) mutants in the phage challenge screen. Data presented as in
1123 Fig 4A. (F) Phage adsorption assay showing enhancement of Loki binding with Δ*gtrOC3* and
1124 Δ*gtrOC4* mutants. Data points show geometric mean ± s.d. (n=3), analyzed by unpaired t-tests
1125 (mutant vs WT). (G-I) *gtrOC*-mediated enhancement of Loki adsorption or killing depends on
1126 capsule. (I) Loki adsorption assay with Δ*gtrOC3,* Δ*itrA*, and double mutant. Data analyzed as in
1127 F (n=3). (H) Plaque formation assay with Δ*gtrOC3,* Δ*itrA*, Δ*gtr6*, and double mutants. (I) Liquid
1128 infection assays with strains in H (n = 3). P values: *, ≤0.05; **, ≤0.01; ***, <0.001. ns, not
1129 significant.
1130
1131 **Supporting information captions**
1132 **S1 Fig. Analysis of Δ*slt* phage susceptibility phenotypes.** (A) Liquid infection assays. WT or
1133 Δ*slt* bacteria were cultured with or without Loki (MOI 1). Data are presented as in Fig 1A (n=3).
1134 (B) Plaque formation assay with Loki spotted onto bottom agar with WT and Δ*slt* bacteria. (C)
1135 Measurement of *rnaA* transcript levels in WT vs Δ*slt* via qRT-PCR. Bars show mean fold change
1136 vs WT ± s.d. (n = 3); analyzed by unpaired t-test. *, P ≤ 0.05.
1137

1138 **S2 Fig. *itrA* complementation analysis with the liquid infection assay.** Bacteria of the noted
1139 genotype were cultured with the indicated level of IPTG with or without Loki at initial MOI of 1.
1140 Growth was measured as in Fig 1A (n = 3).
1141
1142 **S3 Fig. WT ATCC 17978 and Gtr6$^-$ derivatives produce the same levels of capsular**
1143 **polysaccharide.** Bars show mean ± s.d. (n=3); no significant difference among means (P =
1144 0.797, one-way ANOVA). Lanes from a representative gel are shown above the graph.
1145
1146 **S4 Fig. BfmS and LOS-OC mutant hypersusceptibility to Loki depends on capsule**
1147 **biosynthesis.** (A) Phage adsorption assay. Data presented as in Fig. 3G (n=3). (B) Liquid
1148 infection assays. The indicated bacteria were cultured with or without Loki (MOI 1). Data are
1149 presented as in Fig 1A (n=3).
1150
1151 **S5 Fig. Analysis of capsule, Loki susceptibility, and antibiotic sensitivity phenotypes of**
1152 ***rnaA* and DSB mutants.** (A-B) Capsular polysaccharide levels in the indicated strains, grown
1153 with the noted amount of IPTG, were analyzed by SDS-PAGE/Alcian Blue. Complementation of
1154 Δ*rnaA* mutation was tested in A, and Δ*dsbA* was tested in B. "Chr" indicates the chromosomal
1155 mutation; "Plasmid" denotes the gene reintroduced under P(IPTG) control via vector pYDE152,
1156 with - indicating vector with no reintroduced gene. (C) Plaque formation assay. Loki was spotted
1157 onto bottom agar containing WT bacteria harboring pJE101 (IPTG-dependent *dsbA*), with or
1158 without IPTG. (D) Cluster analysis of Tn-seq phenotypic signatures belonging to *bfmS*, *rnaA*,
1159 and *dsb* genes. Heat map shows normalized Tn-seq fitness in z-score units for transposon
1160 mutants in each gene (rows) grown in different conditions (columns) [41]. Dendrogram at left

1161 shows relationship between signatures based on hierarchical clustering. (E) Heat map shows
1162 change in RNA-seq transcript levels in the indicated BfmRS mutant compared to WT control.
1163 Data were extracted from previous datasets [35] and log2 fold change values displayed as heat
1164 map using Prism 9. (F) Liquid infection assays showing functionality of the *rnaA*-msGFP2
1165 fusion construct in Δ*rnaA* mutant bacteria. Bacteria of the indicated genotype were grown
1166 without or with Loki (MOI 1) in the presence or absence of IPTG (1mM), and growth was
1167 measured as in Fig 1A. P values: *, ≤0.05; **, ≤0.01; ***, <0.001.
1168
1169 **S6 Fig. Lon mutation is not associated with increased capsule or Loki adsorption.** (A)
1170 Capsule production by Δ*lon* compared to WT bacteria. Bars show mean ± s.d. (n=3), analyzed by
1171 unpaired t-test. A representative gel is shown above the graph. (B) Phage adsorption assay. Data
1172 points show geometric mean ± s.d. (n=3), analyzed by unpaired t test. P values: *, ≤0.05; ns, not
1173 significant.
1174
1175 **S7 Fig. Analysis of LOS production in altered phage susceptibility mutants bearing**
1176 **mutations in capsule-control loci or *lon*.** LOS production in cell lysates of mutants in *bfmRS*
1177 (A, B) *rnaA* and *dsbA* (C, D) and *lon* (E, F) was analyzed compared to WT control via Pro-Q 300
1178 emerald staining. Representative gels are shown in top panels. Arrowhead indicates location of
1179 novel intermediate band associated with Δ*bfmS* (A). Quantification is shown in bottom panels.
1180 Bars show mean ± s.d. (n=3). Within each set of strains, no significant difference (P > 0.05)
1181 observed in total LOS levels by one-way ANOVA (B, D) or unpaired t-test (F).
1182
1183 **S1 Table. Strains, plasmids, and primers used in this study.**

1184

1185 **S2 Table. Spontaneous *gtr6* mutations conferring phage Loki resistance.**

1186

1187 **S1 Dataset. Loki challenge Tn-seq data.**

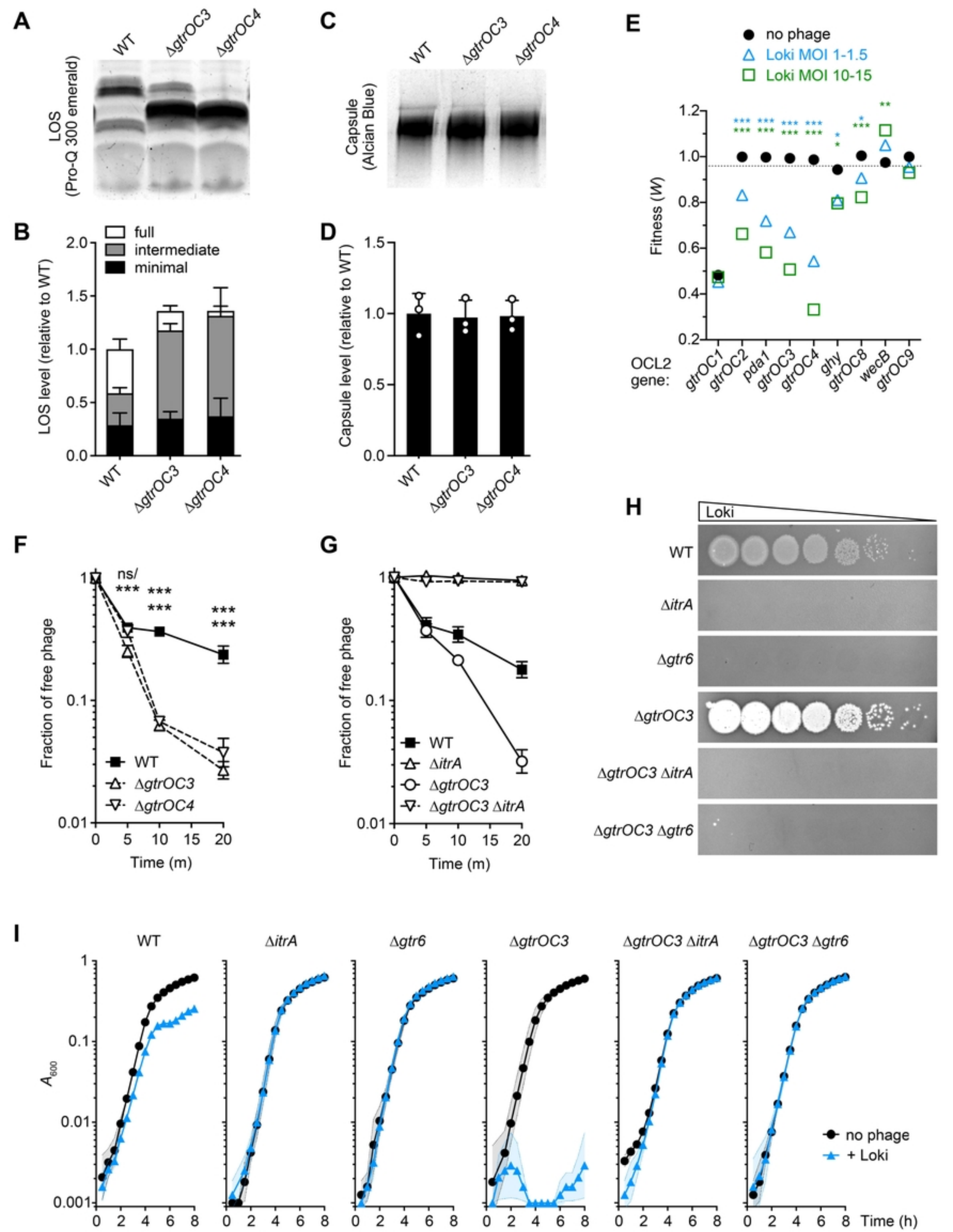
A
WT
ΔgtrOC3
ΔgtrOC4
LOS
(Pro-Q 300 emerald)
B
full
intermediate
minimal
LOS level (relative to WT)
C
Capsule
(Alcian Blue)
D
Capsule level (relative to WT)
E
no phage
Loki MOI 1-1.5
Loki MOI 10-15
Fitness (W)
OCL2
gene:
gtrOC1
gtrOC2
pda1
gtrOC3
gtrOC4
ghy
gtrOC8
wecB
gtrOC9
F
ns/
Fraction of free phage
Time (m)
WT
ΔgtrOC3
ΔgtrOC4
G
ΔitrA
ΔgtrOC3 ΔitrA
H
Loki
Δgtr6
ΔgtrOC3 ΔitrA
ΔgtrOC3 Δgtr6
I
A600
no phage
+ Loki
Time (h)

Fig 8

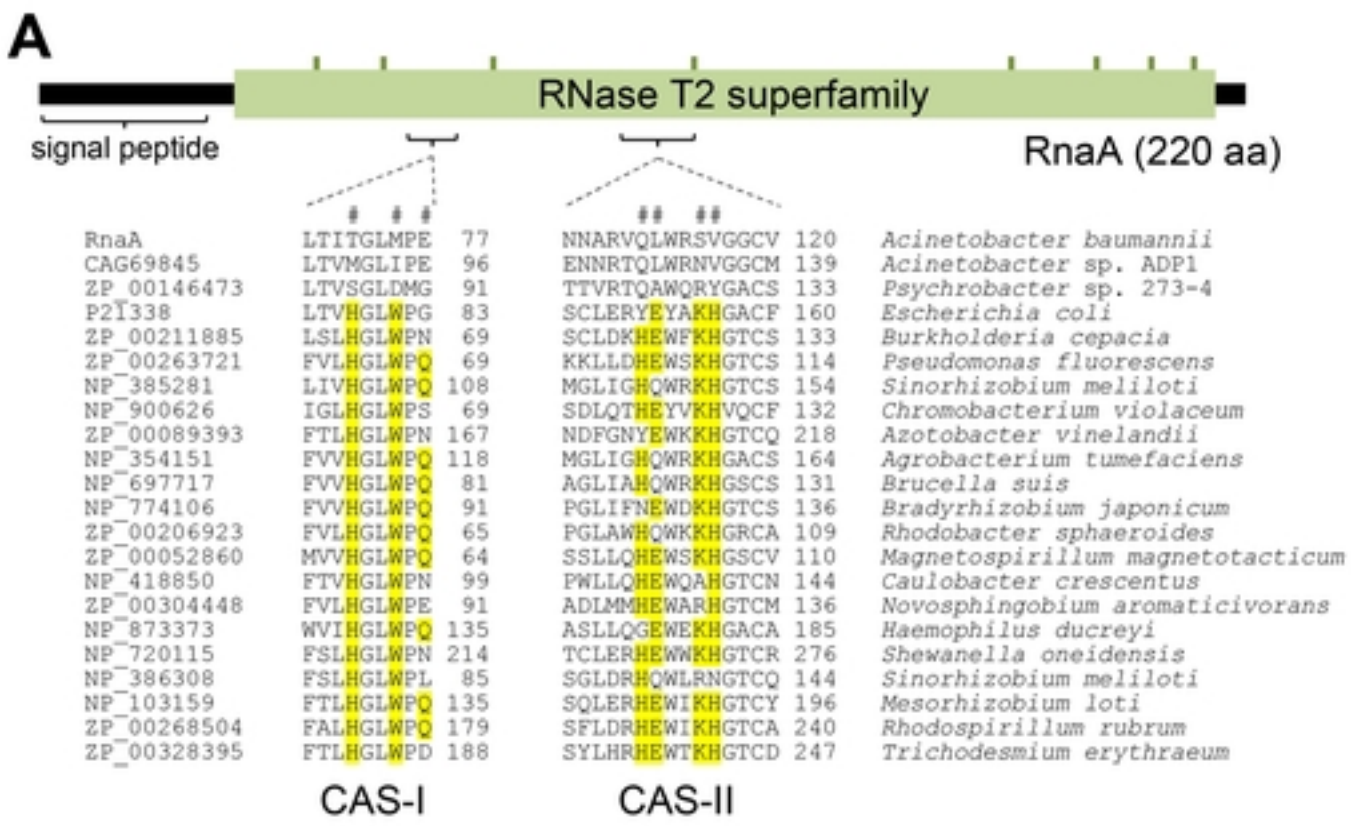
A
RNase T2 superfamily
signal peptide
RnaA (220 aa)
RnaA LTITGLMPE 77 NNARVQLWRSVGGCV 120 Acinetobacter baumannii
CAG69845 LTVMGLIPE 96 ENNRTQLWRNVGGCM 139 Acinetobacter sp. ADP1
ZP_00146473 LTVSGLDMG 91 TTVRTQAWQRYGACS 133 Psychrobacter sp. 273-4
P2I338 LTVHGLWPG 83 SCLERYEYAKHGACF 160 Escherichia coli
ZP_00211885 LSLHGLWPN 69 SCLDKHEWFKHGTCS 133 Burkholderia cepacia
ZP_00263721 FVLHGLWPQ 69 KKLLDHEWSKHGTCS 114 Pseudomonas fluorescens
NP_385281 LIVHGLWPQ 108 MGLIGHQWRKHGTCS 154 Sinorhizobium meliloti
NP_900626 IGLHGLWPS 69 SDLQTHEYVKHVQCF 132 Chromobacterium violaceum
ZP_00089393 FTLHGLWPN 167 NDFGNYEWKKHGTCQ 218 Azotobacter vinelandii
NP_354151 FVVHGLWPQ 118 MGLIGHQWRKHGACS 164 Agrobacterium tumefaciens
NP_697717 FVVHGLWPQ 81 AGLIAHQWRKHGSCS 131 Brucella suis
NP_774106 FVVHGLWPQ 91 PGLIFNEWDKHGTCS 136 Bradyrhizobium japonicum
ZP_00206923 FVLHGLWPQ 65 PGLAWHQWKKHGRCA 109 Rhodobacter sphaeroides
ZP_00052860 MVVHGLWPQ 64 SSLLQHEWSKHGSCV 110 Magnetospirillum magnetotacticum
NP_418850 FTVHGLWPN 99 PWLLQHEWQAHGTCN 144 Caulobacter crescentus
ZP_00304448 FVLHGLWPE 91 ADLMMHEWARHGTCM 136 Novosphingobium aromaticivorans
NP_873373 WVIHGLWPQ 135 ASLLQGEWEKHGACA 185 Haemophilus ducreyi
NP_720115 FSLHGLWPN 214 TCLERHEWWKHGTCR 276 Shewanella oneidensis
NP_386308 FSLHGLWPL 85 SGLDRHQWLRNGTCQ 144 Sinorhizobium meliloti
NP_103159 FTLHGLWPQ 135 SQLERHEWIKHGTCY 196 Mesorhizobium loti
ZP_00268504 FALHGLWPQ 179 SFLDRHEWIKHGTCA 240 Rhodospirillum rubrum
ZP_00328395 FTLHGLWPD 188 SYLHRHEWTKHGTCD 247 Trichodesmium erythraeum
CAS-I
CAS-II
B RnaA-msGFP2
C

Fig 7

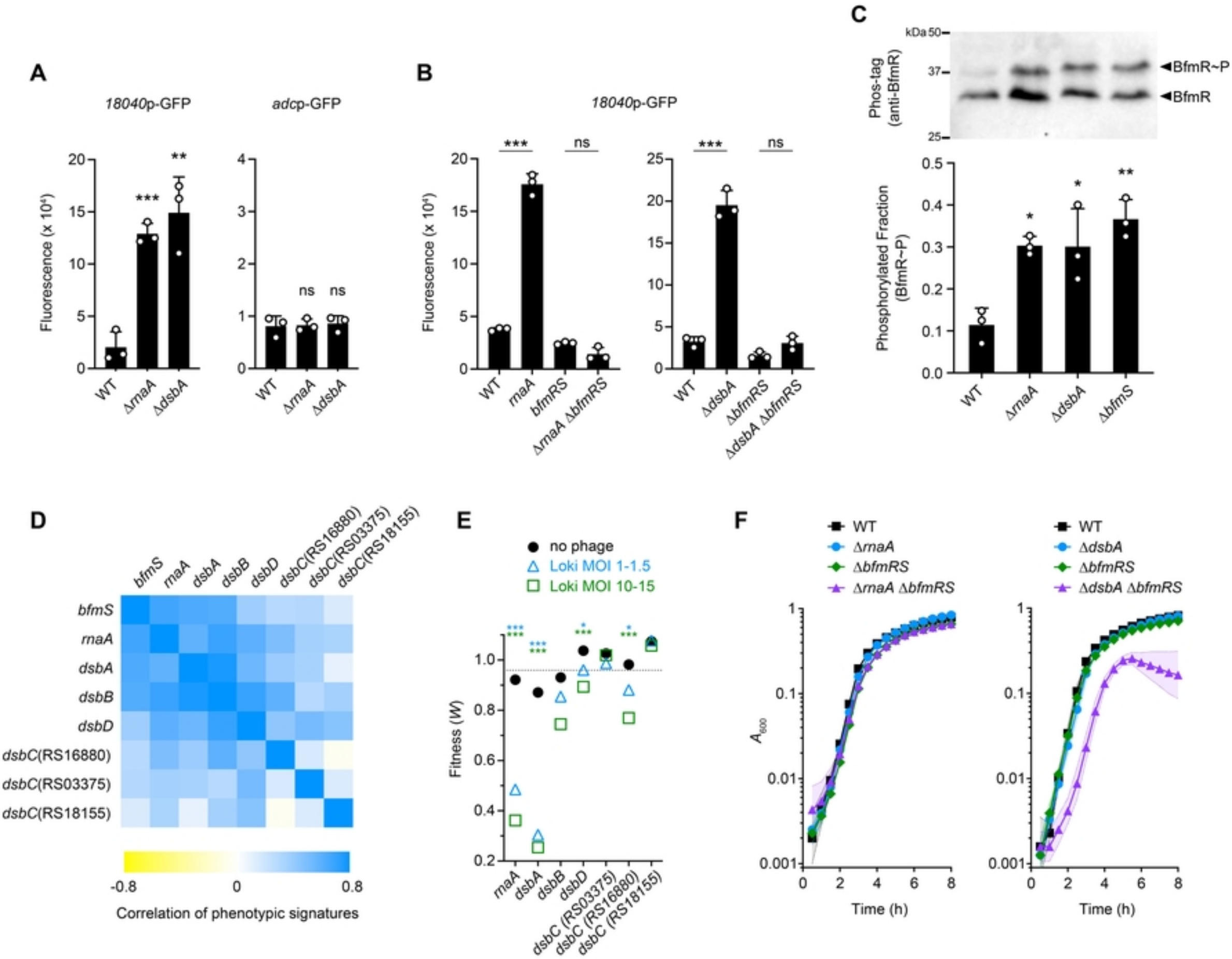
A
18040p-GFP
adcp-GFP
Fluorescence (x 10⁴)
WT
ΔrnaA
ΔdsbA
***
**
ns
B
18040p-GFP
maA
bfmRS
ΔrnaA ΔbfmRS
ΔdsbA
ΔbfmRS
ΔdsbA ΔbfmRS
C
kDa
50
37
25
Phos-tag (anti-BfmR)
BfmR~P
BfmR
Phosphorylated Fraction (BfmR~P)
ΔbfmS
D
bfmS
rnaA
dsbA
dsbB
dsbD
dsbC(RS16880)
dsbC(RS03375)
dsbC(RS18155)
-0.8
0
0.8
Correlation of phenotypic signatures
E
no phage
Loki MOI 1-1.5
Loki MOI 10-15
Fitness (W)
F
A600
Time (h)

Fig 6

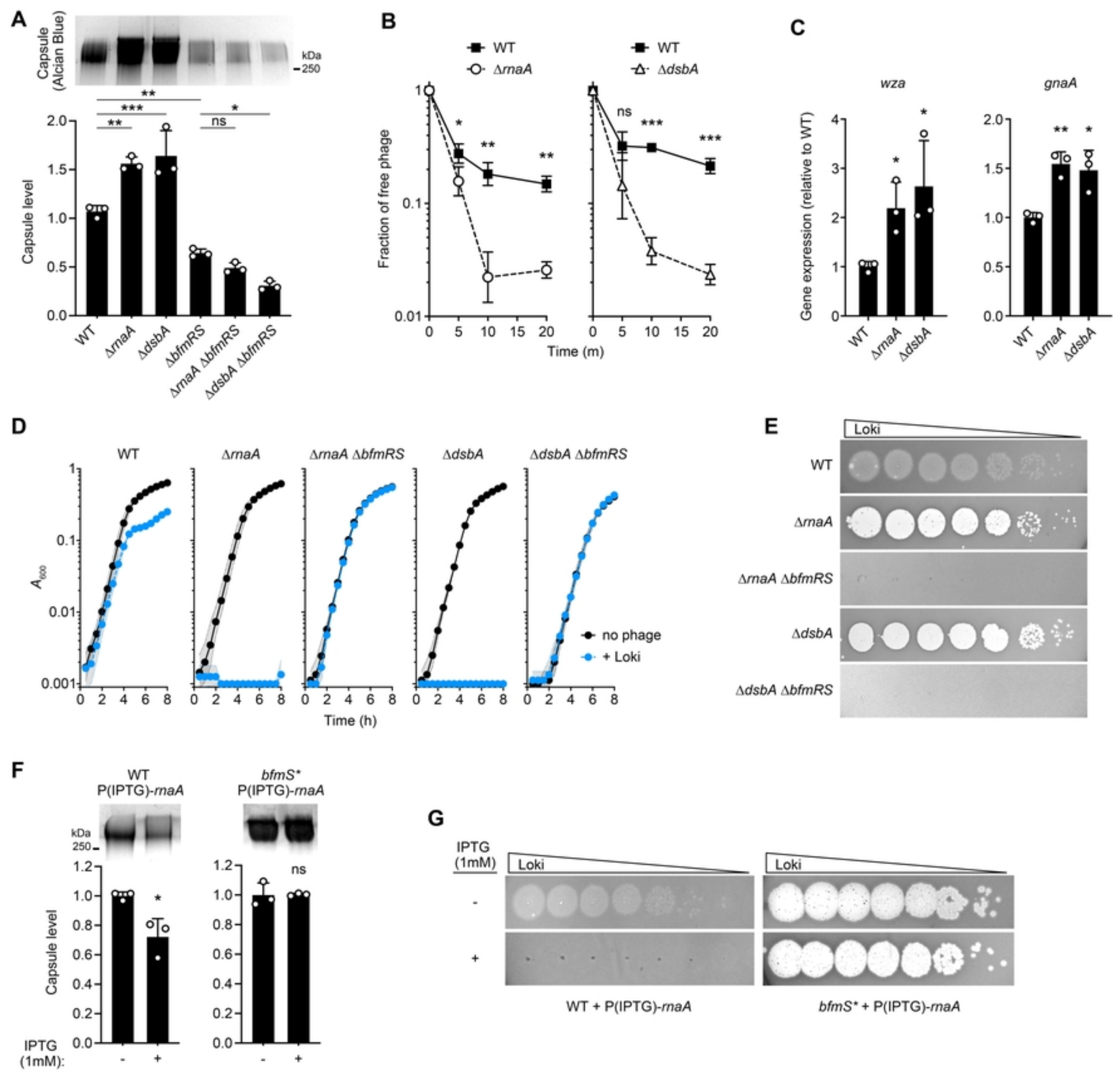
A
Capsule (Alcian Blue)
kDa
250
Capsule level
WT
ΔrnaA
ΔdsbA
ΔbfmRS
ΔrnaA ΔbfmRS
ΔdsbA ΔbfmRS
B
WT
ΔrnaA
ΔdsbA
Fraction of free phage
Time (m)
C
wza
gnaA
Gene expression (relative to WT)
D
WT
ΔrnaA
ΔrnaA ΔbfmRS
ΔdsbA
ΔdsbA ΔbfmRS
A600
Time (h)
no phage
+ Loki
E
Loki
F
WT P(IPTG)-rnaA
bfmS* P(IPTG)-rnaA
IPTG (1mM):
G
IPTG (1mM)
WT + P(IPTG)-rnaA
bfmS* + P(IPTG)-rnaA

Fig 5

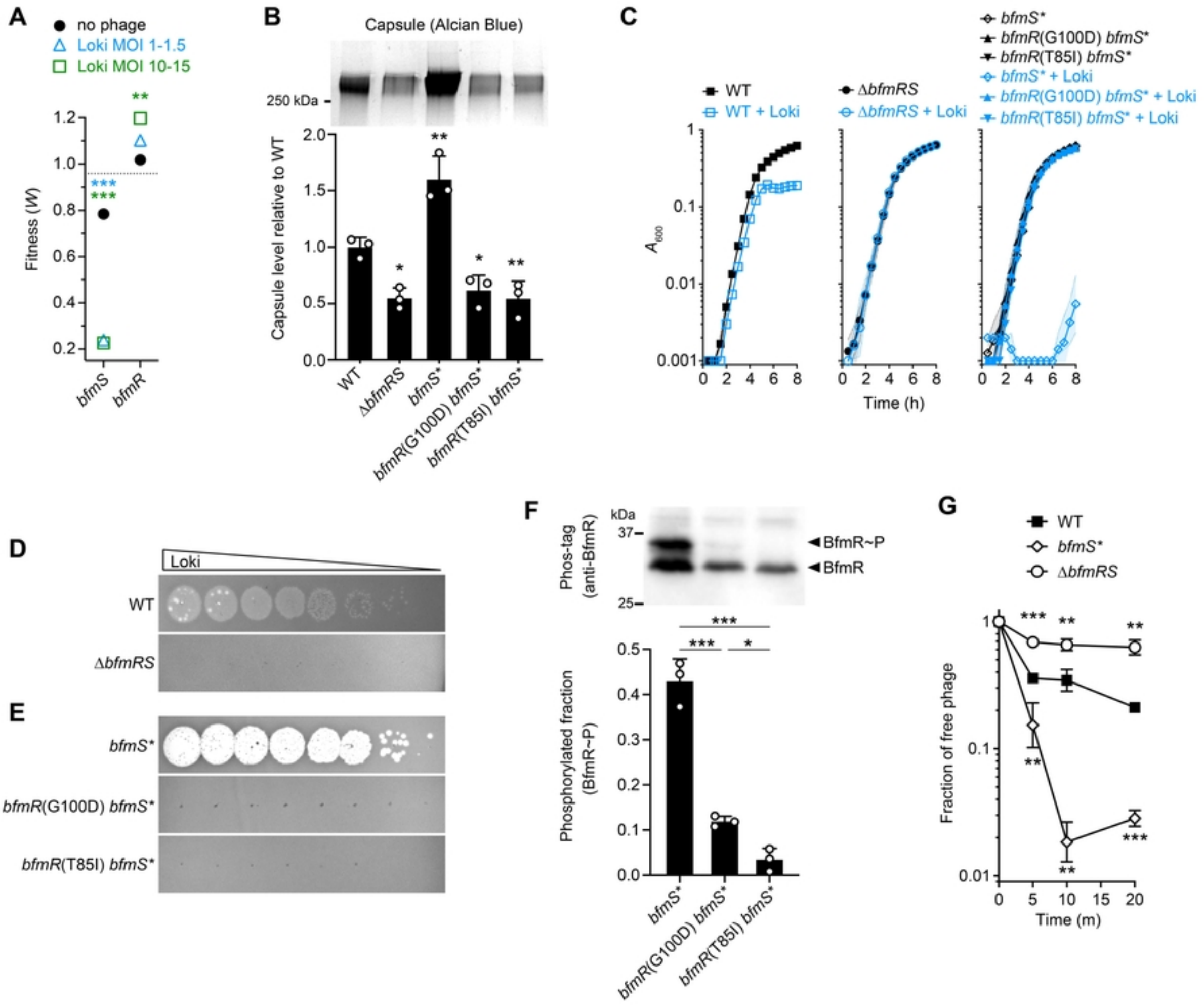
A
no phage
Loki MOI 1-1.5
Loki MOI 10-15
Fitness (W)
bfmS
bfmR
B
Capsule (Alcian Blue)
250 kDa
Capsule level relative to WT
WT
ΔbfmRS
bfmS*
bfmR(G100D) bfmS*
bfmR(T85I) bfmS*
C
WT
WT + Loki
ΔbfmRS
ΔbfmRS + Loki
bfmS*
bfmR(G100D) bfmS*
bfmR(T85I) bfmS*
bfmS* + Loki
bfmR(G100D) bfmS* + Loki
bfmR(T85I) bfmS* + Loki
A600
Time (h)
D
Loki
WT
ΔbfmRS
E
bfmS*
bfmR(G100D) bfmS*
bfmR(T85I) bfmS*
F
Phos-tag (anti-BfmR)
kDa
37
25
BfmR~P
BfmR
Phosphorylated fraction (BfmR~P)
G
WT
bfmS*
ΔbfmRS
Fraction of free phage
Time (m)

Fig 4

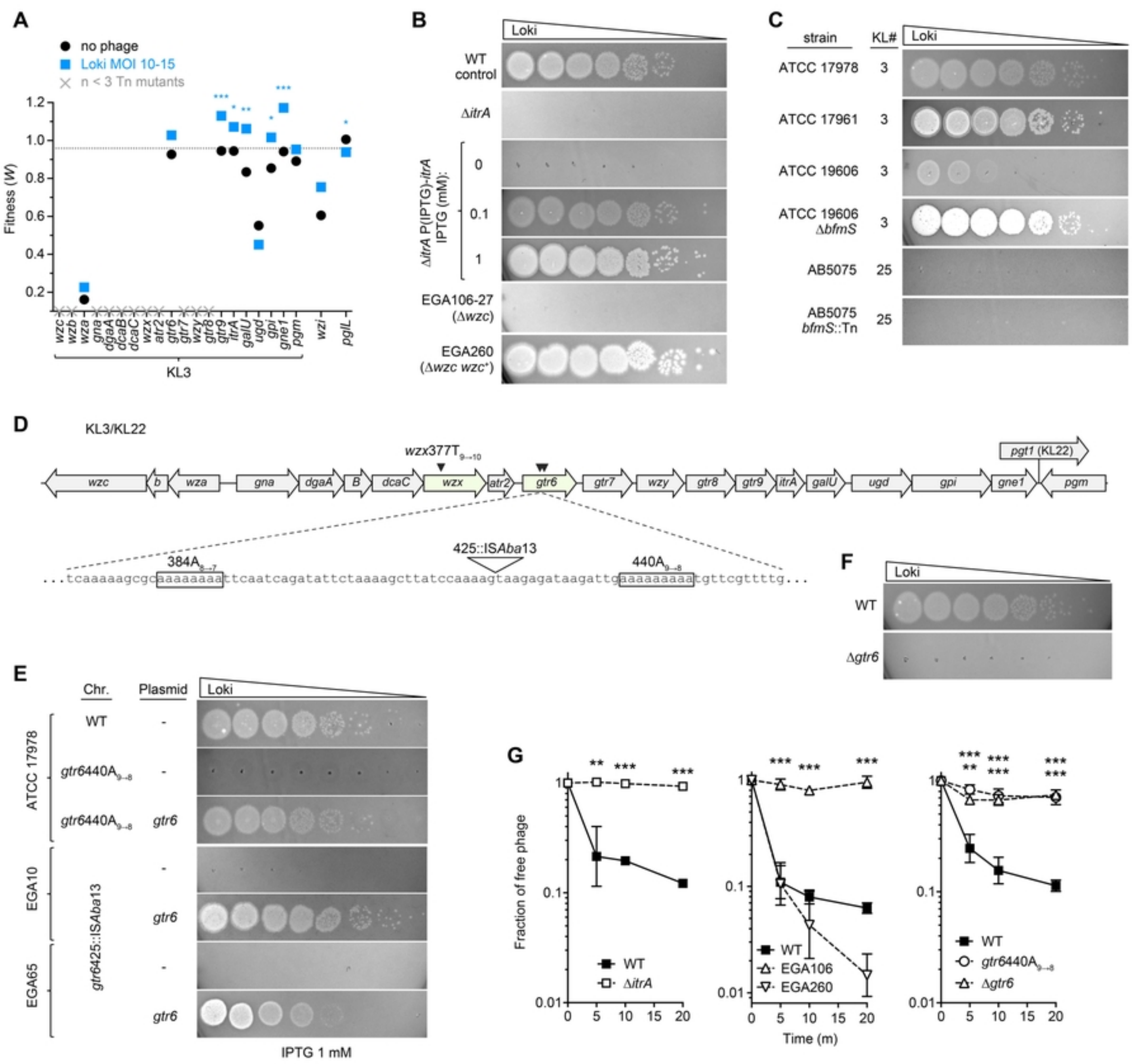
A
no phage
Loki MOI 10-15
n < 3 Tn mutants
Fitness (W)
wzc wzb wza gna dgaA dcaB dcaC wzx atr2 gtr6 gtr7 wzy gtr8 gtr9 itrA galU ugd gpi gne1 pgm wzi pglL
KL3
B
Loki
WT control
ΔitrA
ΔitrA P(IPTG)-itrA IPTG (mM):
0
0.1
1
EGA106-27 (Δwzc)
EGA260 (Δwzc wzc+)
C
strain
KL#
Loki
ATCC 17978 3
ATCC 17961 3
ATCC 19606 3
ATCC 19606 ΔbfmS 3
AB5075 25
AB5075 bfmS::Tn 25
D
KL3/KL22
wzx377T9→10
pgt1 (KL22)
wzc b wza gna dgaA B dcaC wzx atr2 gtr6 gtr7 wzy gtr8 gtr9 itrA galU ugd gpi gne1 pgm
425::ISAba13
384A8→7
440A9→8
...tcaaaaagcgcaaaaaaaattcaatcagatattctaaaagcttatccaaaagtaagagataagattgaaaaaaaatgttcgttttg...
F
Loki
WT
Δgtr6
E
Chr.
Plasmid
Loki
ATCC 17978
WT
gtr6440A9→8
gtr6
EGA10
EGA65
gtr6425::ISAba13
IPTG 1 mM
G
Fraction of free phage
Time (m)
WT
ΔitrA
EGA106
EGA260
gtr6440A9→8
Δgtr6

Fig 3

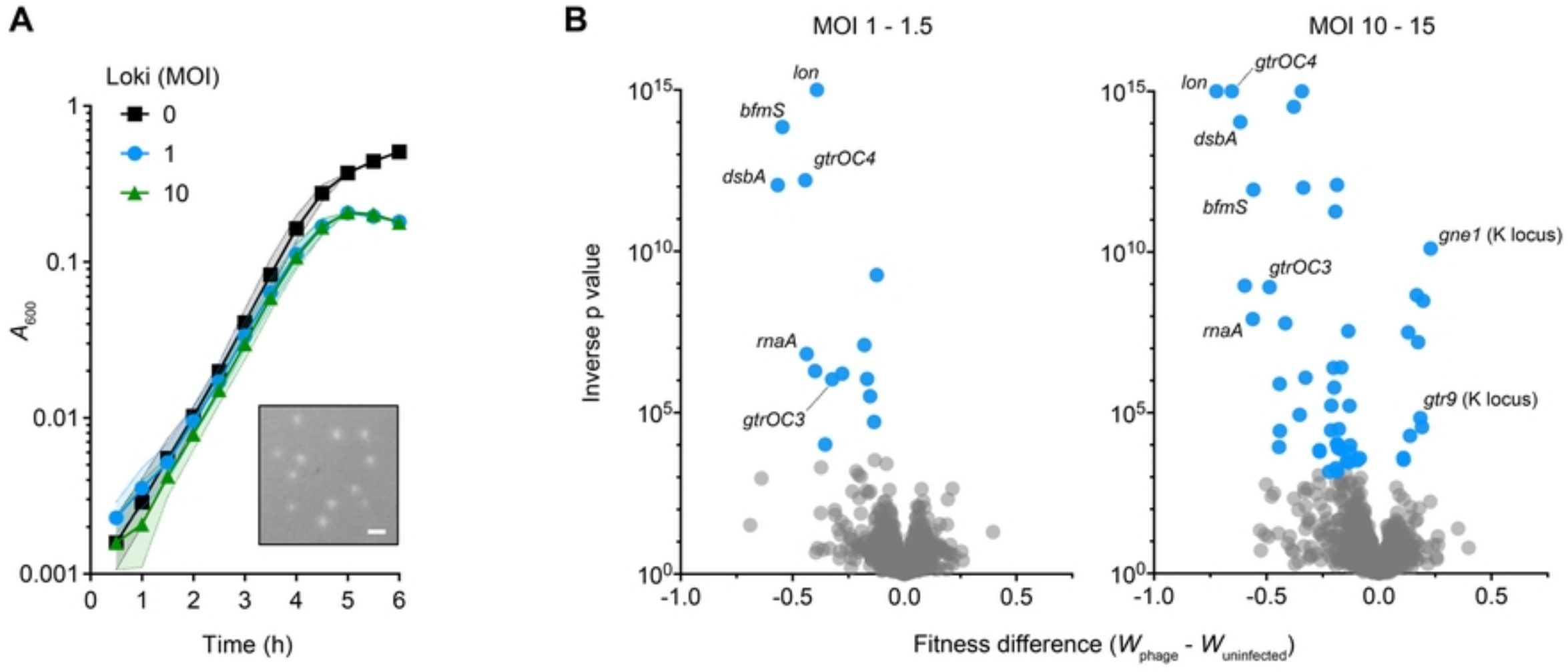
A
Loki (MOI)
0
1
10
$A_{600}$
Time (h)
B
MOI 1 - 1.5
MOI 10 - 15
Inverse p value
lon
bfmS
dsbA
gtrOC4
rnaA
gtrOC3
gne1 (K locus)
gtr9 (K locus)
Fitness difference ($W_{phage}$ - $W_{uninfected}$)

Fig 1

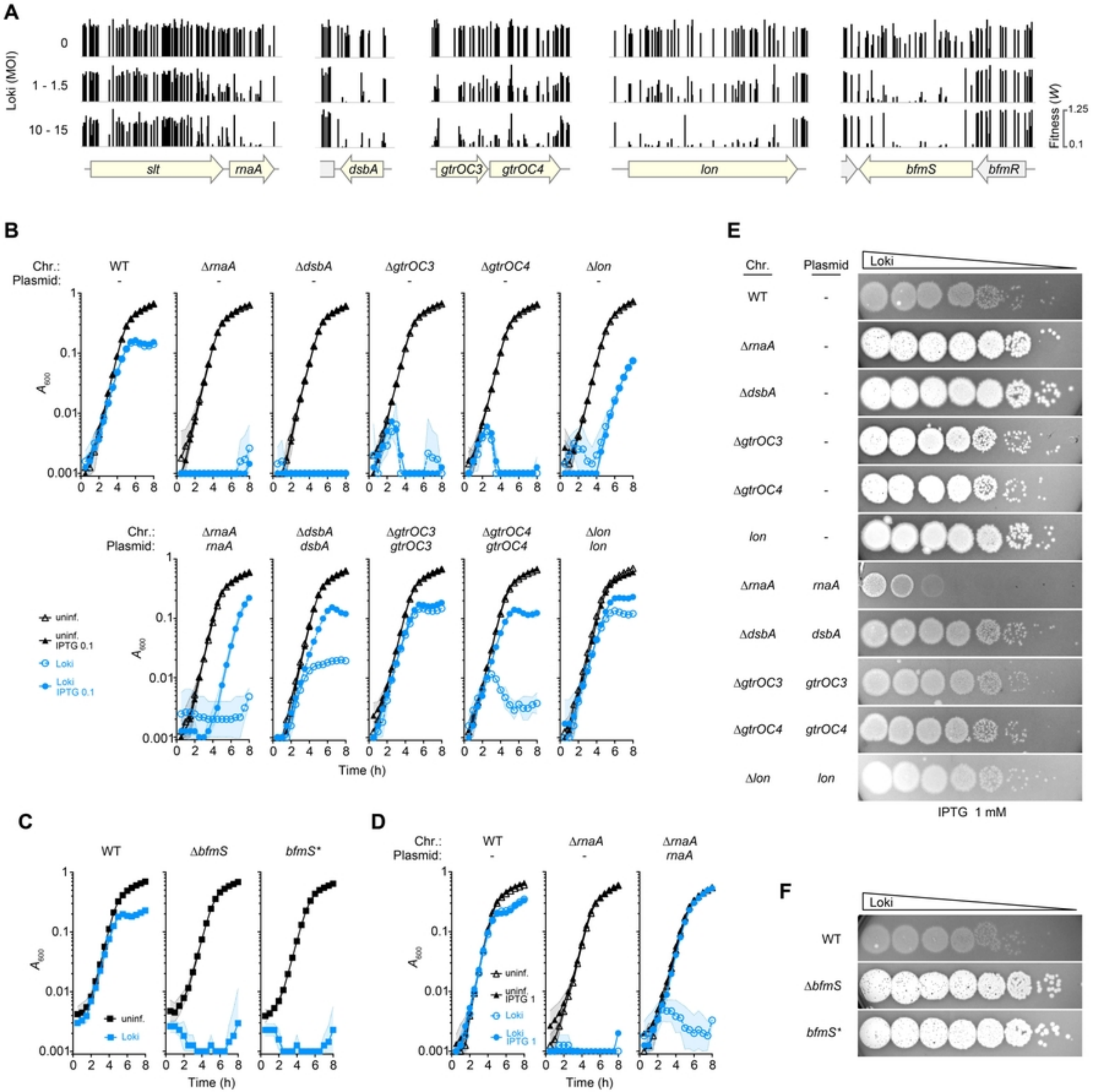
A
Loki (MOI)
0
1 - 1.5
10 - 15
Fitness (W)
1.25
0.1
slt
rnaA
dsbA
gtrOC3
gtrOC4
lon
bfmS
bfmR
B
Chr.:
Plasmid:
WT
ΔrnaA
ΔdsbA
ΔgtrOC3
ΔgtrOC4
Δlon
rnaA
dsbA
gtrOC3
gtrOC4
lon
A600
Time (h)
uninf.
uninf. IPTG 0.1
Loki
Loki IPTG 0.1
C
WT
ΔbfmS
bfmS*
uninf.
Loki
Time (h)
D
Chr.:
Plasmid:
WT
ΔrnaA
ΔrnaA rnaA
uninf.
uninf. IPTG 1
Loki
Loki IPTG 1
Time (h)
E
Chr.
Plasmid
Loki
WT
ΔrnaA
ΔdsbA
ΔgtrOC3
ΔgtrOC4
lon
IPTG 1 mM
F
Loki
WT
ΔbfmS
bfmS*

Fig 2